

## AN ABSTRACT OF THE DISSERTATION OF

Joshua Thomas Hargraves for the degree of Doctor of Philosophy in Radiation Health Physics presented on May 17, 2023.

Title: Advancements in Phytoremediation, Dosimetry, and Environmental Radiological Protection: Integrating Endemic Plants, Anatomically Accurate Phantoms, and Real-world Data for Improved Assessments

Abstract approved: \_\_\_\_\_

Kathryn A. Higley

The environmental impact of the nuclear industry has prompted the need for innovative remediation strategies and accurate radiological assessments. This paper synthesizes three studies that collectively explore the potential of endemic plant species for phytoremediation, the development of anatomically accurate phantoms for precise dosimetry calculations, and the critical evaluation of International Commission on Radiological Protection (ICRP) guidelines using in situ plant analyses. The first study investigates phytoremediation at legacy uranium mining sites in the Colorado Plateau, focusing on endemic plant species such as *Sporobolus airoides*, *Helianthus petiolaris*, *Kochia scoparia*, and *Atriplex canescens*. The second study scrutinizes the environmental radiological protection guidelines proposed in ICRP Publications 108 and 136 through the lens of in situ plant analyses, revealing the potential for refining the Reference Animals and Plants (RAPs) approach and dose coefficients. Lastly, the third study introduces FSOPhantom, an open-source software designed for generating anatomically accurate phantoms from CT and MRI images, producing a novel dosimetric model for the common banana (*Musa acuminata Colla*) as an example. By integrating innovative remediation strategies, anatomically accurate dosimetry models, and real-world data, this research aims to enhance the assessment and management of radiological contamination, ultimately contributing to more effective environmental protection and public health outcomes.

©Copyright by Joshua Thomas Hargraves  
May 17, 2023  
CC BY 4.0

Advancements in Phytoremediation, Dosimetry, and Environmental Radiological  
Protection: Integrating Endemic Plants, Anatomically Accurate Phantoms, and Real-  
world Data for Improved Assessments

by  
Joshua Thomas Hargraves

A DISSERTATION

submitted to

Oregon State University

in partial fulfillment of  
the requirements for the  
degree of

Doctor of Philosophy

Presented May 17, 2023  
Commencement June 2023

Doctor of Philosophy dissertation of Joshua Thomas Hargraves presented on May 17, 2023.

APPROVED:

---

Major Professor, representing Radiation Health Physics

---

Head of the School of Nuclear Science and Engineering

---

Dean of the Graduate School

I understand that my dissertation will become part of the permanent collection of Oregon State University libraries. My signature below authorizes release of my dissertation to any reader upon request.

---

Joshua Thomas Hargraves, Author

## ACKNOWLEDGEMENTS

I would like to extend my heartfelt gratitude to my advisor, Dr. Kathryn Higley, for hearing out a nervous student wanting to pursue a PhD one summer afternoon. In addition, I would like to extend my thanks to Dr. Elizabeth Ruedig for her words of encouragement and advice when I was first getting started on my research, and by extension to Dr. Leah Minc for her expertise leading to the refining of my methodology for study.

To my family, who have supported me in ways I cannot even begin to account, thank you for inspiring me to always stay curious. To my loving wife, who followed my dream to come to the other side of the country and keeps me sane, thank you for always being the foundation and inspiration for my thoughts and dreams.

I would like to extend a thank you to the composer Akihiko Narita for developing a piece of music that accompanied my writing through my exams and this dissertation- if an exam is truly a dragon, you have helped me survive it. And finally, to all of my friends and family of Moulton 213, especially Cody Lis, Raymond Meyer, Sean Gonzalez, Amanda Whiteside, Nick Likeum, Alexander Logisz, and Evan Becker- for always being there for a review, a joke, or a game in the best and worst of times.

# TABLE OF CONTENTS

	<u>Page</u>
1 General Introduction	1
2 The Bioconcentration of Radionuclides in Endemic Plants of the Southwest United States	3
2.1 Introduction	4
2.2 Methods	8
2.2.1 Sample Preparation Information	8
2.2.2 Gamma Spectroscopy	12
2.2.3 Reference for Gamma Spectroscopy	14
2.2.4 Neutron Activation Analysis	15
2.2.5 Reference for Neutron Activation Analysis	17
2.2.6 Bioconcentration Factor and Translocation Factor	18
2.3 Results & Discussion	19
2.4 Conclusion	31
2.5 Acknowledgements	32
3 Growing Concerns: An Evaluation of ICRP Publications 108 and 136 Via Analysis of Endemic Plants of the Southwest United States	39
3.1 Introduction	41
3.2 Methods	43
3.2.1 The Reference Grass	43
3.2.2 In Situ Species	45
3.3 Results & Discussion	49
3.3.1 Uranium Comparisons	51

## TABLE OF CONTENTS (Continued)

	<u>Page</u>
3.3.2 Thorium Comparisons	53
3.3.3 Radium Comparisons	55
3.3.4 Derived Consideration Reference Levels	56
3.4 Conclusion	58
3.5 Acknowledgements	59
4 Banana For Scale: An analysis of voxelized phantoms of the banana for use in dosimetric modeling	63
4.1 Introduction	65
4.2 Methods	67
4.2.1 Voxel Overview	67
4.2.2 Computational Modeling Programs	68
4.2.3 Post MRI Modelling of Plant Tissues	70
4.2.4 Generating a “Reference” Banana	77
4.2.5 FSOPhantom Specifications	80
4.3 Results & Discussion	82
4.3.1 Ellipsoidal Reference Model	83
4.3.2 Three Part Banana Model	87
4.4 Conclusion	108
4.5 Acknowledgements	109
5 General Summary and Conclusions	112

## LIST OF FIGURES

<u>Figure</u>	<u>Page</u>
2.1 Grants Mining District.	6
2.2 Example of lysimeter construction.	12
3.1 Example of lysimeter construction.	47
4.1 Biological Drawing of a Cross Section of a Banana.	71
4.2 Example of a first pass of segmentation in 3DSlicer, highlighting the colloquial skin, flesh, and central reproductive structure as separate structures.	72
4.3 Example of “step” anomalies in segmentation of a volume due to a limitation in slices along a plane.	73
4.4 Semi-smoothed meshes preserving geometry of the internal meat and reproductive network overlaid across each other in Meshmixer.	75
4.5 An ellipsoidal model of a “Reference” Banana conforming to the idealized dimensions of the nearest rectangular prism from a scan of a real banana.	78
4.6 Absorbed Fractions to reference ellipsoid tissue for gamma and electron sources located in the center of the ellipsoid tissue.	86
4.7 Absorbed Fractions to various segmented tissues compared to the reference ellipsoidal phantom for gamma sources located in the ‘internals’ tissues.	91
4.8 Absorbed Fractions to various segmented tissues compared to the reference ellipsoidal phantom for electron sources located in the ‘internals’ tissues.	93
4.9 Absorbed Fractions to various segmented tissues compared to the reference ellipsoidal phantom for gamma sources located in the mesocarp tissues.	98
4.10 Absorbed Fractions to various segmented tissues compared to the reference ellipsoidal phantom for electron sources located in the mesocarp tissues.	100
4.11 Absorbed Fractions to various segmented tissues compared to the reference ellipsoidal phantom for gamma sources located in the epicarp tissues.	105
4.12 Absorbed Fractions to various segmented tissues compared to the reference ellipsoidal phantom for electron sources located in the epicarp tissues.	107

## LIST OF TABLES

<u>Table</u>	<u>Page</u>
2.1 An overview of the abundance of species across sites and their frequency of growth measured by extracted pulls per identified clusters of growth.	10
2.2a Soil physical characteristics for Sections 17, 22, and 35 soil media.	21
2.2b Soil physical characteristics for Sections 17, 22, and 35 soil media.	23
2.3 Summary of BCF and TF results for Radium-226 in plants grown in relevant soil media. Blank spaces denote values below detectable limits.	24
2.4 Summary of BCF and TF results for Uranium-238 in plants grown in relevant soil media. Blank spaces denote values below detectable limits.	27
2.5 Summary of BCF and TF results for Thorium-232 in plants grown in relevant soil media. Blank spaces denote values below detectable limits.	29
3.1 The dimensions of an ellipsoid conforming to the spike of Reference Grass.	44
3.2 Estimated internal dose rates in plant tissues from <sup>238</sup> U laden media using the dose rate equation in ICRP 108 and the results of dose per calculated bioconcentration factors. Blank spaces denote values below detectable limits.	51
3.3 Estimated internal dose rates in plant tissues from <sup>232</sup> Th laden media using the dose rate equation in ICRP 108 and the results of dose per calculated bioconcentration factors. Blank spaces denote values below detectable limits.	53
3.4 Estimated internal dose rates in plant tissues from <sup>226</sup> Ra laden media using the dose rate equation in ICRP 108 and the results of dose per calculated bioconcentration factors. Blank spaces denote values below detectable limits.	55
3.5 Comparison of the total dose rates calculated as the sum of the internal and external dose rates for all radionuclides of concern, differentiated by Site and method of calculation.	57
4.1 Dimensions of the various segments generated as STL meshes for study in FSOPhantom.	76
4.2 The dimensions of an ellipsoid conforming to the nearest rectangular prism from a scan of a real banana, for use as a “Reference” Banana.	79

## LIST OF TABLES (Continued)

<u>Table</u>	<u>Page</u>
4.3 The material density of the various segments of the banana component tissues alongside the elemental compositions of each, including: C, O, N, H, Cl, K, Mn, Fe, Cu, Zn, Br, Rb, Sr in the Epicarp, with the loss of Ca in the Mesocarp, and ICRU material for the internal combination.	81
4.4a The output of running FSOPhantom over an idealized reference banana phantom, consisting of ICRU 4 Tissue for gamma sources.	83
4.4b. The output of running FSOPhantom over an idealized reference banana phantom, consisting of ICRU 4 Tissue for electron sources.	84
4.5a Mean Dose, Absorbed Fractions for a variety of gamma sources of varying energies initially spawned in the “Internals” tissue.	88
4.5b Mean Dose, Absorbed Fractions for a variety of electron sources of varying energies initially spawned in the “Internals” tissue. For runs that did not return viable data, ‘-’ is used.	89
4.6a Mean Dose, Absorbed Fractions for a variety of gamma sources of varying energies initially spawned in the Mesocarp tissue.	95
4.6b Mean Dose, Absorbed Fractions for a variety of electron sources of varying energies initially spawned in the Mesocarp tissue.	96
4.7a Mean Dose, Absorbed Fractions for a variety of gamma sources of varying energies initially spawned in the epicarp tissue.	102
4.7b Mean Dose, Absorbed Fractions for a variety of electron sources of varying energies initially spawned in the epicarp tissue. For runs that did not return viable data, ‘-’ is used.	103

## Chapter 1: General Introduction

The implications of the nuclear industry and its subsequent environmental impact have long been a topic of concern for communities, governments, and private stakeholders. The increasing need for cost-effective and ecologically sustainable remediation strategies, along with a more accurate understanding of radiological dose and environmental radiological protection, has motivated researchers to explore innovative approaches. This paper ties together three studies that focus on (1) phytoremediation using endemic plant species, (2) the development of anatomically accurate phantoms for precise dosimetry calculations, and (3) a critical assessment of International Commission on Radiological Protection (ICRP) guidelines using in situ plant analyses.

The first study investigates the potential for phytoremediation at uranium mining sites in the Colorado Plateau using endemic plant species, such as *Sporobolus airoides*, *Helianthus petiolaris*, *Kochia scoparia*, and *Atriplex canescens*. By evaluating these species for uranium, thorium, and radium concentrations in their tissues, this research aims to aid in establishing a low-cost, ecologically stable, and low-maintenance remediation strategy.

The second study scrutinizes the environmental radiological protection guidelines proposed in ICRP Publications 108 and 136 through the lens of in situ plant analyses. By comparing the actual dose rates of various plant species grown in contaminated soil to those proposed in the ICRP guidelines, this research highlights the need for refining the Reference Animals and Plants (RAPs) approach and dose coefficients based on real-world data to

enhance the accuracy and reliability of environmental radiological protection assessments while also acknowledging the validity of the tools that have been implemented thus far.

Finally, the third study introduces FSOPhantom, an open-source software designed to bridge the gap between image collection and radiation transport calculation. Coupled with the medical image analysis software 3D Slicer, FSOPhantom enables the generation of anatomically accurate phantoms from CT and MRI images for more precise dosimetry assessments. The software's utility is demonstrated through the creation of a novel dosimetric model for the common banana (*Musa acuminata Colla*), a plant of particular interest in the radiation professional community.

These three studies collectively emphasize the importance of integrating innovative remediation strategies, anatomically accurate dosimetry models, and real-world data in addressing the challenges posed by the nuclear industry and its associated environmental risks. The insights gleaned from this integrated approach are poised to significantly improve the assessment and management of radiological contamination, ultimately contributing to more effective environmental protection and public health outcomes.

Chapter 2:  
The Bioconcentration of Radionuclides in Endemic Plants of the  
Southwest United States

Joshua Hargraves

Kathryn Higley

Nuclear Science and Engineering, Oregon State University

This manuscript has been submitted to Health Physics, May 2023.

## ABSTRACT

Historically, uranium mining in the United States was prolific throughout the Colorado Plateau. These sites contributed toward technological and community development; however, their environmental legacies currently face ire from community, government, and private shareholders. Current methods of remediation or coverage are cost-prohibitive and ecologically damaging. Phytoremediation of select sites using endemic species is an ecologically stable, low maintenance, and relatively inexpensive methodology for remediation or potential waste cover design. Select species such as: *Sporobolus airoides*, *Helianthus petiolaris*, *Kochia scoparia*, and *Atriplex canescens*, at one such site were evaluated for uranium, thorium, and radium concentrations in respective tissues.

### 2.1 INTRODUCTION

While much consideration has been granted toward the study of humans in work environments, relatively few studies have been conducted regarding the ecosystems wherein these industries and endeavors are situated. Furthermore, when these industries leave the area, the ecosystem, let alone the general populace still in residence, is often left behind in consideration. One example is the Grants Mineral Belt, a subdivision of the larger uranium mining belt that proliferates the southwestern Colorado Plateau. The region of interest (ROI)

pursuant with this work, Ambrosia Lake, was the site of uranium mining from the 1950s through the 1980s, establishing a mining industry that dominated the local economy until multiple closures culminating with the end of the uranium mining recessions in the United States in 1982-1983 (EPA, 2011). The town of Grants, NM, which was prior labeled as the “Uranium Capital of the World” quickly became a post-mining-boom town, and much of the land was ceded back to the Navajo Nation and the Laguna Pueblo, with the town proper being redubbed as an agricultural industry belt and home for retirees. Yet, the region is prone to misuse and disuse in various forms: The town of Grants has had a significant downward economic spiral since the closure of the mines and the populace still has great disdain for the nuclear industry and region (Johansen, 2011; Sorrentino, 2016). In addition, multiple accounts of wild stock grazing rights and water rights usage requests within the ROI by native reservations reopened the region to further inquiry regarding safety of the land’s use in 2007. These requests culminated in legitimate concerns over contamination in the environment spanning from the head of Rio Puerco to the lower grasslands, with the potential for detrimental effects on not only the general population but also in their livestock and growth stock. Further concern is added when the native nations have been under advisement since 1983 to not use the graze lands within the ROI for lack of uptake data regarding contaminants remaining from the mining activities of the past from both water and plants. This has been met with both apprehension and distrust of the nuclear, albeit mining, industry as a result. The native nations and the



include data on particular radionuclides, plants of study are not endemic in nature, there is not widely studied segmentation of plant growth transfer factors, and variant concentration gradient bands have not been reviewed. The lack of study relating to endemic life can lead to ignorance of environmental effects in the most positive scenario, or gross disregard to uptake to fauna in lieu of humans in the worst scenario. Therefore, a more thorough analysis of the region's endemic plant life should take precedence over common cereals, roots, legumes, and fruits to better understand the ecological impact of specific radionuclides on the environment. Segmentation of plants into their roots and shoots for these endemic species will allow for a better calculation of fractional uptake of contaminants in the ROI; hence, well defined Transfer Ratios/Bioconcentration Factors (BCF), or the concentration of contaminants in plant sections from soil, will be discussed. Finally, an established review of any correlative effect between a gradient of concentrations in the soil to the fractional uptake in the plants grown in said soil would be significant to remediation studies.

Two contaminants of interest were identified by the current stakeholder and legacy site claim holder, Broken Hill Proprietary (BHP). These were Radium-226 and Uranium-238, with another contaminant, Thorium-232, being of tertiary relevance. The determination of plant uptake, specifically the transfer ratios between plant sections from soil, could further inform the relationship between contaminant concentration and environmental retention. This has potential applications in extrapolating the measured

concentration ratios to sites with varying amounts of contamination (Beresford, 2016; Vandenhove, 2007). Beyond application of concentration ratios, the radionuclide uptake potential of endemic plants is of vital importance to advancing studies in phytoremediation, both as a monetary resource and as an ecological level competitive analysis (Lavergne, 2004; Mendez, 2008).

To this end, soils were acquired in 2018 and in 2019 after establishing a near-linear gradient of cumulative concentration ( $R^2 = 0.93$ ) across three sites within the area of study. Per the nomenclature of the stakeholder and as can be seen in Figure 2.1, Sections 17, 22, and 35 were used. Section 22 was found to have the lowest surface activity measured by a handheld gamma scintillator surface activity monitor, at ~24 (cps), section 17 at ~75 (cps), and finally section 35 at ~215 (cps). In addition to soil sampling along these sites, a collection of plants was collected from each region, with the goal of identifying the best candidate species for later study of uptake.

## 2.2 METHODS

### 2.2.1 Sample Preparation Information

Soil was excavated from the sites with shovels from the surface to a maximum depth of 15 cm to capture the topsoil (to represent the area of concern for contamination and human health risk, as well as the zone of interest for plant

growth for the phytoremediation study). The bulked soil sample was placed into thick contractor garbage bags inside of United States Shipping Grade plastic buckets, filling approximately three quarters of each bucket. The internal containment bags were securely closed with zip-ties. A maximum of 110 gallons (416 L) of soil was collected to meet UN 2910 Hazardous Shipper Restrictions. Shipping containers were inspected before leaving the site by swiping, at minimum, a 10-cm<sup>2</sup> area on the exterior of the container and analyzed with a scintillation counter in the on-site Environmental Restoration Group (ERG) office. Sample containers were driven from the field site near Grants, NM to the shipping facility in Albuquerque, NM, before being relocated to the Oregon State University campus in Corvallis, OR. The containers were stored in the Oregon State University Radiation Center at room temperature until use.

After cross-referencing plant species across extraction locations, four candidate plants for uptake studies were identified from the following criteria alongside Table 2.1: Proliferation across sites, proliferation within respective sites, and literature data on uptake in similar media. From these criteria four species of plants were chosen for lysimeter uptake study: Alkali Sacaton (*Sporobolus airoides*), Prairie Sunflower (*Helianthus petiolaris*), Summer Cypress (*Kochia scoparia*), and Fourwing Saltbush (*Atriplex canescens*). Of note, other invasive species were also present as seeds in the soil, providing some opportunistic data on Indian Mustard (*Brassica juncea*) and Common Dandelion (*Taraxacum officinale*).

**Table 2.1.** An overview of the abundance of species across sites and their frequency of growth measured by extracted pulls per identified clusters of growth.

Plant Species	Present in Section	Total Extractions of Species
Fourwing Saltbush ( <i>Atriplex canescens</i> )	17, 22, 35	20
Yellow Rabbitbrush ( <i>Chrysothamnus viscidiflorus</i> )	17	10
Mounding Peppergrass/Mountain Pepperweed ( <i>Lepidium montanum</i> )	17	5
Broom Snakeweed ( <i>Gutierrezia sarothrae</i> )	17, 35	10
Blue Grama ( <i>Bouteloua gracilis</i> )	17, 35	10
Inland/Desert Saltgrass ( <i>Distichlis stricta</i> )	35	6
Curlycup Gumweed ( <i>Grindelia squarrosa</i> )	22, 35	10
Winterfat ( <i>Krascheninnikovia lanata</i> )	22	10
Globemallow ( <i>Sphaeralcea ambigua</i> )	22	10
Prairie Sunflower ( <i>Helianthus petiolaris</i> )	22, 35	6
Galletta ( <i>Hilaria jamesii</i> )	22	10
Hoary Aster ( <i>Dieteria canescens</i> )	35	5
Summer Cypress ( <i>Kochia scoparia</i> )	35	10
Alkali Sacaton ( <i>Sporobolus airoides</i> )	17, 35	15
Salt Cedar ( <i>Tamarix chinensis</i> )	35	5
Western Wheat Grass ( <i>Agropyron smithii</i> var. <i>smithii</i> )	35	5

Seeds were procured from a variety of commercial retailers from outside the site. Lysimeters were used for analysis of plant growth and translocation of contaminants. While concerns over the validity of greenhouse growth versus in situ growth have been addressed in prior literature, replicates of lysimeters per site and per plant can normalize some of the inconsistencies between in situ growth and greenhouse work (Gerzabek, 1998; Islam, 2011). The versatility of small scale lysimeters has been found to be applicable, more so in high clay soils such as those worked with here (Kay, 2005; Ruth, 2018).

The study was conducted within a locked greenhouse enclosure at the Radiation Center in order to secure the radioactive soil. The greenhouse enclosure can house approximately five lysimeters per species (10 cm diameter x 25 cm height ABS pipe columns (~2.059 L) filled approximately 80% with the contaminated soil from Section 17, 22, and 35 without combination with the remainder being filled with pea gravel and filter meshing to aid drainage) for 20 lysimeters total, as can be seen in Figure 2.2. Water added to plants was conducted daily at approximately 100 mL.

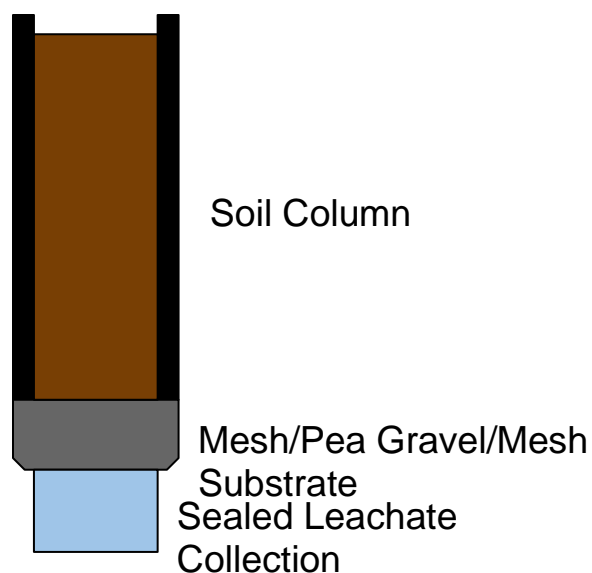


**Figure 2.2.** Example of lysimeter construction.

Plants were cleaned of particulate matter after growth to germination stage. A deionized water rinse was followed by a microfiber tissue scouring to remove potentially contaminating soil media. Dried plants were ground in a SPEX Mixer/Mill and buffered with a cellulose binder of a similar particulate size to achieve a geometry similar to that of the calibration source (Bollinder, 1997; Cuske, 2014).

### 2.2.2 Gamma Spectroscopy

Radium-226 was measured via its progeny, Radon-222 (Half-life = 3.8 d), following 20 days of ingrowth to produce an equilibrium with products Lead-214 (Half-life = 28.6 m) and Bismuth-214 (Half-life = 19.7 m). These were measured via gamma spectroscopy using High-Purity Germanium detectors (HPGe) to evaluate the 352 keV (37.6%) gamma ray of Lead-214 and the 609

keV (46.1%) gamma ray of Bismuth-214, both of which are averaged to estimate the Radium-226 activity. This is necessary due to the overlap of the 186 keV peaks derived from both Uranium-238 and Radium-226 (EML, 2018; IAEA, 2010; Jia, 2012; Nelson, 2014). Additionally, uranium measurement correction of radium concentrations are further complicated when uranium concentrations and thorium concentrations far exceed those of radium concentrations, or when samples containing all three are not properly sealed to allow disequilibrium, further skewing the potential of correction on the 186 keV line. (Déjeant, 2014).

Our current methodology is built upon the work found in Nelson et al. where no wet chemistry is required, only low heating of the plant or soil to remove excess contaminant moisture. To this end, samples were desiccated at 100°C in an oven until a mass stabilization was achieved indicating a full water loss. Samples were placed in 237 mL natural polypropylene jars (VWR 89027-989), filled to approximately 10mm above the bottom of the container, for a ~10-15 g fill. In the case of plant material, this geometry was achieved by buffering and homogenizing the samples with SPEX Cellulose Binder 3642. Samples were sealed with a compression foam-insert screw-top lid and secured further in Ziploc Sandwich bags and allowed to sit in a climate controlled, dry environment at room temperature. The determination of Radium-226 in environmental solids by gamma spectrometry has long been based on the detection of emissions of the radon progeny (Radon-222) nuclides, i.e., Lead-214 and Bismuth-214 after an ingrowth period of at least

20 days, during which the sample has been hermetically sealed to ensure secular equilibrium between Radium-226 and its progeny. It is necessary to undertake the measurement not long after equilibrium has been achieved due to the progeny isotopes short half-lives (IAEA, 2010).

Thus, the samples were set for 20-25 days to achieve equilibrium between gaseous Radon-222, a progeny of Radium-226, and the further progeny Bismuth-214 and Lead-214. After this ingrowth period, samples are placed on the top, flat face of a HPGe detector and a spectrum is collected over a 24-hour period. This spectrum is analyzed at the requisite peaks associated with the energies of the gammas emitted by Lead-214 and Bismuth-214, and a Compton Continuum correction averaged over five relative maxima calculations were performed to achieve the approximate counts.

### 2.2.3 Reference for Gamma Spectroscopy

For validation of Radium-226, the following quality control and quality assurance (QA/QC) information is available. In 2020, the ND ( Non-Detection Level) for Radium-226 on the HPGe was determined to be 33 counts to 35 counts, depending on the HPGe array used. All calibration standards were prepared with the same matrix as the samples and were prepared fresh post ingrowth before each analysis. Soil samples from the International Atomic Energy Agency (IAEA) were run prior to spectra analysis of plant and soil

samples and an internal standard (background) was used during analysis on the HPGe to ensure accuracy. The IAEA samples have an acceptance range of 80%-120%. The following quality control soil samples from IAEA were available (stored in a climate controlled dry room): Standard Reference Material (SRM) 448 (IAEA, 2013). Quality control samples were processed and analyzed before the samples to verify the spectra efficiency and the precision and accuracy of the measurements by the HPGe. Samples were measured over a 24-hour period. Calibration curves are run within the range of the sample concentrations to ensure low-level and high-level concentration measurement accuracy. The original data report printouts from the HPGe analyses are retained for data reduction, data entry, and verification. Sample dilutions by buffer are considered before reporting the results. For calculation of a mean when values are below detection, data is omitted. All samples were mixed properly into a homogeneous state prior to analysis.

#### 2.2.4 Neutron Activation Analysis

For Neutron Activation Analysis, ashed plant tissue is required to reduce both the mass and volume of organic compounds and pre-concentrate other elements, thereby increasing analytical sensitivity (Harju et al. 2004; Koh et al. 1999; Lalor et al. 2003). Plant tissue was desiccated in a laboratory oven at 100C until a mass equalization occurs indicating a full water loss. To dry ash the samples, approximately 5-25 g of plant material (depending on

availability) was placed in a covered porcelain crucible and heated to 550°C. in a muffle furnace, using a slow ramp of ca. 200°C per hour and a soak time of 20 hours. As soon as samples are cool enough to handle, the ash is lightly ground and homogenized using a ceramic mortar and pestle and transferred to tightly capped liquid scintillation vials to prevent re-hydration. Concentration factors are determined from the ratio of pre-fire to post-fire mass and used to determine the equivalent mass of un-ashed plant material that was irradiated.

Desiccated and ashed samples were extracted in ~1000mg allotments and placed in LAContainers Polyvials and sealed with a thermal clamp, before then being placed in a larger Polyvial and doubly sealed. Samples are then placed in an automated system that allows for the samples to be exposed to the output of the Oregon State University TRIGA Reactor's neutron flux, irradiating and activating the samples. After the irradiation, the characteristic gamma rays emitted by the decaying radionuclides are quantitatively measured by HPGe semiconductor radiation detectors, and the gamma rays detected at a particular energy are usually indicative of a specific radionuclide's presence, in this instance activated Neptunium-239 indicating the presence and concentration of  $^{238}\text{U}$  (Landsberger, 2012; Zaidi, 1999). Similarly, Thorium-232 was deduced from the activation of  $^{233}\text{Pa}$  (Pulhani, 2000). Data reduction of gamma ray spectra by means of a computer analysis then yields the concentrations of various other elements in samples being studied.

### 2.2.5 Reference for Neutron Activation Analysis

All calibration standards were prepared with the same matrix as the samples and were prepared fresh before each analysis. Plant and soil samples from the National Institute of Standards and Technology (NIST) were activated in tandem with plant and soil samples and an internal standard was used during analysis on the INAA to ensure accuracy. The NIST samples have an acceptance range of 80%-120%. The following quality control soil and plant samples from NIST were available (stored in a climate controlled dry room): Standard Reference Material (SRM) 1547, Cellulose Binder 3642, and 1570a (NIST, 2014; NIST, 2022; SPEX, 2022). Quality control samples were processed and analyzed with the samples to verify the activation efficiency and the precision and accuracy of the measurements by the INAA. Soil samples are activated in triplicate and values obtained from INAA analysis are an average of three replicate readings per sample. Included in the analysis are the digest blanks and laboratory blanks to verify there is no sample cross contamination. Activated duplicates are included to ensure reproducibility. Calibration curves were run within the range of the sample concentrations to ensure low-level and high-level concentration measurement accuracy. The original data report printouts from the INAA analyses were retained for data reduction, data entry, and verification by the analyst. Sample dilutions were considered before reporting the results. For calculation of a mean when values are below detection, data was omitted. All samples were mixed properly prior

to analysis.

### 2.2.6 Bioconcentration Factor and Translocation Factor

The ideal result for candidates for phytoremediation is a transfer ratio known as a Bioconcentration Factor (BCF) of  $\geq 1$ , indicating a transfer of contaminants from growth media to plant tissues (Zhang, 2002). Depending on the post phytoremediation method for extraction of plant material for disposal or reuse, a higher BCF in the shoot meristematic tissue than the root meristematic tissue may be ideal. A BCF of  $\geq 1$  for only the meristematic root tissue indicates a candidate likely suited for phytostabilization rather than phytoremediation. This ratio is calculated with the following expression:

$$BCF = \frac{\text{Concentration in Plant Tissues}}{\text{Concentration in Growth Media}}$$

Where the ratio is applicable to roots, stems, and leaves of studied plants (Mishra, 2019).

Concurrently, the calculation of the Translocation Factor (TF), or the ability for a plant to translocate contaminants from root tissues to shoot tissues, identifies a plant useful for phytoextraction, or full phytoremediation of contaminants through agricultural cultivation and extraction (Nirola, 2015).

This ratio is calculated with the following expression:

$$TF = \frac{\text{Concentration in Plant Shoot Tissues}}{\text{Concentration in Plant Root Tissues}}$$

Where the ratio is again applicable to roots, stems, and leaves of studied plants (Mishra, 2019).

### 2.3 RESULTS & DISCUSSION

Plants are expected to have the majority of contaminants or trace constituent uptake within their root structure, with secondary uptake in their shoots (Hewamanna, 1988; Padmavathiamma, 2007; Singh 2005). However, this may vary based on the contaminant or other soil factors (Soudek, 2007; Vandenhove, 2009).

Soils from the three test sites were studied at the Central Analytical Laboratory on the Oregon State University campus. Per Table 2.2a, Section 17 was characterized as sandy soil, with Sections 22 and 35 being predominantly clay. Organic matter (OM) was lowest in Section 17 but was a medium grade in Sections 22 and 35, compared to the overall one percent standard in New Mexico.

Soil characteristics, such as texture, organic matter content, and mineral composition, can have a significant impact on the mobility of radionuclide contaminants and water movement.

For instance, the texture of soil, which is determined by the size of its particles, affects the movement of water and solutes through the soil. Sandy soils have larger pores between particles and tend to be well-drained, allowing

water and contaminants to move more quickly through the soil. In contrast, clay soils have smaller pores and are often more compact, which can slow down water movement and increase the retention of contaminants. The organic matter content of soil also plays a role in radionuclide mobility and water movement: it can bind with contaminants, reducing their mobility in the soil and can increase water-holding capacity in the soil, which can influence the movement of contaminants by reducing their leaching potential. Mineral composition of soil can also affect the mobility of radionuclide contaminants, potentially acting as sorbents, adsorbing the contaminants and reducing their mobility in the soil, or as competitive intakes, with Ca and Ra potentially filling the same biological function as chemical analogs in OM.

Potentially Mineralizable Nitrogen was low across all sites compared to the state average, with Active Carbon being particularly low across all sites relative to the average one to four percent that is ideal for plant growth.

**Table 2.2a.** Soil physical characteristics for Sections 17, 22, and 35 soil media.

Section	Sand	Silt	Clay	Water Stable Aggregates	C	N	OM	Active C	CO2	CO2	Potentially Mineralizable Nitrogen		
									Respiration 24 hr	Respiration 96 hr			
	%	%	%	%	%	%	ppm	$\mu\text{g CO}_2\text{-C g}^{-1}\text{ dry soil day}^{-1}$	$\mu\text{g CO}_2\text{-C g}^{-1}\text{ dry soil day}^{-1}$	ppm NO3-N t0	ppm NO3-N t28	mg N kg <sup>-1</sup> soil day <sup>-1</sup>	
17	77	10	13	15.4	0.92	0.03	1.83	107	13	8	7.08	12.53	0.2
22	26	34	40	15.8	1.07	0.08	2.14	187	19	11	17.13	27.51	0.3
35	21	26	48	31.4	1.37	0.1	2.74	216	52	29	24.01	40.31	0.6

The pH across sites was moderately alkaline, ranging from 8.05 to 8.77, typical values for arid and semiarid environments. As expected of clay soils, the cation exchange capacity (CEC) was higher than the sandy soils of Section 17. Table 2.2b also notes the non-salinity of the soils per the low electrical conductivity (EC) across sites. Other available nutrient values such as phosphorus, potassium, and magnesium were measured and found to be in tolerable ranges for the arid soil, though the levels of calcium indicate the potential for highly calcareous soil media that inhibits root formation.

**Table 2.2b.** Soil chemical characteristics for Sections 17, 22, and 35 soil media.

Section	pH	EC	P	K	Ca	Mg	K	Ca	Mg	CEC	Ra	U	Th
	pH	dS m <sup>-1</sup>	ppm	ppm	ppm	ppm	meq 100g <sup>-1</sup>	meq 100g <sup>-1</sup>	meq 100g <sup>-1</sup>	meq 100g <sup>-1</sup>	Bq kg <sup>-1</sup>	ppm	ppm
17	8.77	0.3	30.3	192	5117	120	0.49	25.58	1.00	27	536.13	117.37	4.89
22	8.36	0.47	24.4	680	5834	453	1.74	29.17	3.77	35	21.78	12.02	12.93
35	8.05	0.66	49	458	6279	421	1.17	31.4	3.51	36	408.77	199.96	11.76

**Table 2.3.** Summary of BCF and TF results for Radium-226 in plants grown in relevant soil media. Blank spaces denote values below detectable limits.

Plant Species	BCF Sec. 17 Radium-226	TF Sec. 17 Radium-226	BCF Sec. 22 Radium-226	TF Sec. 22 Radium-226	BCF Sec. 35 Radium-226	TF Sec. 35 Radium-226
<i>Sporobolus airoides</i>	$0.83 \pm 0.40$	$0.37 \pm 0.56$	$3.46 \pm 2.31$	$0.77 \pm 0.32$	$0.57 \pm 0.29$	$0.26 \pm 0.30$
<i>Helianthus petiolaris</i>	$0.49 \pm 0.18$	$0.81 \pm 0.43$	$2.69 \pm 2.24$	$0.09 \pm 0.09$	$0.42 \pm 0.36$	$0.17 \pm 0.15$
<i>Kochia scoparia</i>	$0.29 \pm 0.10$	$0.60 \pm 0.08$	$2.40 \pm 0.01$	$0.13 \pm 0.01$	$1.07 \pm 0.61$	$0.38 \pm 0.13$
<i>Atriplex canescens</i>	$0.57 \pm 0.49$	$0.79 \pm 0.55$	$1.41 \pm 1.04$	$0.33 \pm 0.47$	$0.10 \pm 0.03$	$0.81 \pm 0.51$
<i>Brassica juncea</i>	-	-	$0.92 \pm 0.33$	-	-	-
<i>Taraxacum officinale</i>	-	-	-	-	$0.63 \pm 0.13$	$0.22 \pm 0.07$

For Radium-226, there was no ideal phytostabilizing plant in Section 17 soil media, with *A. canescens* having the most potential per Table 2.3. In Section 22 soil media, *S. airoides* had the highest uptake by plant mass, but *K. scoparia* was the most statistically stable BCF, though each other species met the criteria of having a BCF greater than one. In Section 35, only *K. scoparia* showed evidence of phytostabilization potential. These findings corroborate the 1980 investigation by Marple for *A. canescens* and *K. scoparia* grown on uranium mill tailings, however the TF values provide new insights into the effectiveness of these plants for phytoremediation given sufficient time. With Section 17 soil, *H. petiolaris* imparts a significant fraction of the radium salt into its shoot section, whereas *S. airoides* shows potential for phytoremediation in Section 22 soil media. *A. canescens* demonstrates the only measured plant with phytoremediation potential in Section 35 soil within statistical bounds.

A statistical analysis via ANOVA-Bonferroni review of the variation of concentrations of uranium, thorium, and radium species between Sections 17, 22, and 35 determined that the concentrations of thorium and uranium did not meet the level of evidence necessary to merit separate study of Sections 17 and 35, thus only one section of data was used as comparison to Section 22.

Uranium-238 uptake across the three sites was modeled as seen in Table 2.4, with *H. petiolaris* demonstrating the strongest case of phytostabilizing potential, *A. canescens* being of secondary notice. No species met the sufficient levels to be considered a phytostabilizer at Section 35. The

TF of *S. airoides* showed evidence for being a potent phytoextractor in Section 22 soil, but the statistical variation present between samples does not foster evidence for consistent results, likewise for *H. petiolaris*. *K. scoparia* did, however, demonstrate unique statistically consistent TF in Section 22 soil media among intended endemic species, with the opportunistic *B. juncea* also showing signs of statistically strong TF potential. In Section 35, only *S. airoides* demonstrated TF potential for Uranium-238 but was statistically variable in being a viable candidate for phytoextraction.

**Table 2.4.** Summary of BCF and TF results for Uranium-238 in plants grown in relevant soil media. Blank spaces denote values below detectable limits.

Plant Species	BCF Sec. 22 Uranium-238	TF Sec. 22 Uranium-238	BCF Sec. 35 Uranium-238	TF Sec. 35 Uranium-238
<i>Sporobolus airoides</i>	$0.58 \pm 0.39$	$9.27 \pm 10.56$	$0.46 \pm 0.23$	$2.63 \pm 3.22$
<i>Helianthus petiolaris</i>	$3.47 \pm 1.59$	$1.61 \pm 1.19$	$0.46 \pm 0.33$	$0.71 \pm 0.67$
<i>Kochia scoparia</i>	$0.59 \pm 0.01$	$2.09 \pm 0.06$	$0.41 \pm 0.03$	$0.19 \pm 0.01$
<i>Atriplex canescens</i>	$1.16 \pm 0.09$	$0.30 \pm 0.08$	-	-
<i>Brassica juncea</i>	$0.26 \pm 0.00$	$1.04 \pm 0.00$	-	-

Thorium-232 uptake across the three sites was modeled as seen in Table 2.5. *H. petiolaris* was the sole plant species that noted potential for phytostabilization in Section 22 soil, though each measured plant species showed potential for phytoremediation by translocation of material to the shoot sections, if statistically unstable. Grown in Section 35 soil media, only *S. airoides* demonstrated potential evidence for phytostabilization, and no measured plants indicated the ability to remediate.

**Table 2.5.** Summary of BCF and TF results for Thorium-232 in plants grown in relevant soil media. Blank spaces denote values below detectable limits.

Plant Species	BCF Sec. 22 Thorium-232	TF Sec. 22 Thorium-232	BCF Sec. 35 Thorium-232	TF Sec. 35 Thorium-232
<i>Sporobolus airoides</i>	$0.37 \pm 0.20$	$8.85 \pm 10.18$	$1.03 \pm 0.07$	$0.14 \pm 0.01$
<i>Helianthus petiolaris</i>	$2.17 \pm 1.83$	$4.04 \pm 4.23$	$0.10 \pm 0.03$	$0.69 \pm 0.35$
<i>Kochia scoparia</i>	$0.11 \pm 0.01$	$2.38 \pm 1.79$	$0.19 \pm 0.17$	$0.24 \pm 0.25$
<i>Atriplex canescens</i>	$0.14 \pm 0.09$	$1.04 \pm 0.85$	-	-
<i>Brassica juncea</i>	$0.08 \pm 0.01$	$1.12 \pm 0.01$	-	-

The significant variation in BCFs and TFs across plants and across sites further confounds the data, which is likely caused by the variation in the physical and chemical structure of each site. As noted, prior, Section 17 contained far sandier relative soil than that of Sections 22 and 35. Sandy soils (Section 17) are well-drained with larger pores, while clay soils (Sections 22 and 35) have smaller pores and are more compact, impacting water and contaminant movement. Organic matter content in soils can also bind with contaminants, especially the biological analogs like radium, reducing their mobility, and increasing water-holding capacity, influencing contaminant leaching potential. The mineral composition can also affect the mobility of radionuclides by acting as sorbents or competitive intakes. For example, if a soil is rich in calcium (Ca) and radium (Ra) ions, both may compete for the same binding sites on soil minerals or organic matter. The presence of high concentrations of competing ions can reduce the likelihood of radionuclide sorption, potentially increasing their mobility in the soil. On the other hand, if a soil is relatively low in competing ions, radionuclides may be more likely to bind to available sites and be immobilized. Additionally, there are matrix differences between the calibration sources which were soil based for radium and a hybrid plant matrix for thorium and uranium that may further skew the results.

Additionally, this paper seeks to understand the variation between root and shoot tissues for the first time in these endemic plants, which has shown with the above evidence that whole plant uptake fractions may not have the

efficacy needed to understand the phytoremediation of plant species.

## 2.4 CONCLUSION

The availability of endemic species to be utilized in phytostabilization and phytoremediation shows potential, with some distinct variation between sites and among concentration bands. In particular *H. petiolaris*, *S. airoides*, and *K. scoparia* had defining features of prominent BCF and TF values in varying conditions, underlying the importance of selecting species best suited for regions of reclamation. This study found that different plant species demonstrated varied phytostabilization and phytoremediation potential in different soil media, based on their BCFs and TFs. These differences can be attributed to the unique soil characteristics at each site, which affect the mobility and availability of contaminants for plant uptake. The effectiveness of these plants for phytoremediation is also influenced by these soil factors, as well as the specific plant species' abilities to take up and translocate contaminants within their tissues. The soil of the arid region poses challenges to the scalability of remediation or stabilization efforts, but the potential for relatively low cost and environmentally friendly techniques are of paramount importance to developing long lasting solutions for the surrounding communities and the biodiversity therein.

## 2.5 ACKNOWLEDGEMENTS

This work was supported by Broken Hill Proprietary. The author would like to thank Dr. Elizabeth Ruedig for the advice and support in site acquisition, as well as the invaluable skills of Dr. Leah Minc for her expertise with INAA and sample preparation.

## REFERENCES

- Beresford NA, Wood MD, Batlle JV, Yankovich TL, Bradshaw C, Willey N.  
Making the most of what we have: Application of extrapolation  
approaches in radioecological wildlife transfer models. *J Environ  
Radioact.* 2016;151:373-386. doi:10.1016/j.jenvrad.2015.03.022
- Bolinder MA, Angers DA, Dubuc JP. Estimating shoot to root ratios and  
annual carbon inputs in soils for cereal crops. *Agric Ecosyst Environ.*  
1997;63(1):61-66.
- Chen S, Zhu Y, Hu Q. Soil to plant transfer of  $^{238}\text{U}$ ,  $^{226}\text{Ra}$  and  $^{232}\text{Th}$  on a  
uranium mining-impacted soil from southeastern China. *J Environ  
Radioact.* 2005;82(2):223-236. doi:10.1016/j.jenvrad.2005.01.009
- Cuske M, Karczewska A, Gałka B. Ultrasonic cleaning of plant roots in their  
preparation for analysis on heavy metals. *Zeszyty Naukowe. Inżynieria  
Środowiska/Uniwersytet Zielonogórski.* 2014.
- Déjeant A, Bourva L, Sia R, Galois L, Calas G, Phommavanh V, Descostes  
M. Field analyses of  $^{238}\text{U}$  and  $^{226}\text{Ra}$  in two uranium mill tailings  
piles from Niger using portable HPGe detector. *J Environ Radioact.*  
2014;137:105-112. doi: 10.1016/j.jenvrad.2014.06.012
- EML HASL-300 Method Ra-03-RC: Radium-226 in Soil, Vegetable Ash,  
and Ion Exchange Resin. 2018. Available from:  
<https://www.epa.gov/homeland-security-research/eml-hasl-300->

method-ra-03-rc-radium-226-soil-vegetable-ash-and-ion

- EPA. Aerial Radiological Surveys Ambrosia Lake Uranium Mines  
Ambrosia, NM. United State Environmental Protection Agency. 2011.
- Gerzabek MH, Strebl F, Temmel B. Plant uptake of radionuclides in  
lysimeter experiments. *Environ Pollut.* 1998;99(1):93-103.
- Harju L, Rajander J, Saarela KE, Lill JO, Heselius SJ, Lindroos A. Losses of  
elements during dry ashing of biological materials. 10th International  
Conference of Particle Induced X-ray Emission and its Analytical  
Applications, PIXE 2004, Portoroz, Slovenia. June 4-8, 2004.  
Available from: <http://pixe2004.ijs.si/>.
- Hewamanna R, Samarakoon CM, Karunaratne, PAVN. Concentration and  
chemical distribution of radium in plants from monazite-bearing soils.  
*Environ Exp Bot.* 1988;28(2):137-143.
- IAEA. Analytical methodology for the determination of radium isotopes in  
environmental samples. IAEA/AQ/19, pp. 6-7. 2010.
- IAEA. Certified Reference Material IAEA-448: Soil from Oil Field  
Contaminated with Technically Enhanced Radium-226. IAEA/AQ/30.  
2013.
- Islam M, Mao S, M Shahidul Alam A, Eneji A, Hu Y, Xue X. A Lysimeter  
Study for Leaching Losses, Sustainable Fertilization, and Growth  
Responses of Corn (*Zea mays* L.) Following Soil Amendment with a  
Water-Saving Superabsorbent Polymer. *Appl Eng Agric.* 2011;27:757-  
764. doi:10.13031/2013.39575.

- Jia G, Jia J. Determination of radium isotopes in environmental samples by gamma spectrometry, liquid scintillation counting and alpha spectrometry: A review of analytical methodology. *J Environ Radioact.* 2012;106:98-119. doi:10.1016/j.jenvrad.2011.12.003
- Johansen BE. The High Cost of Uranium in Navajoland. Amizade. 2011. Available from: <https://amizade.org/wp-content/uploads/2011/07/B-Johansen-High-Cost-of-Uranium.doc>.
- Kay P, Blackwell PA, Boxall, AB. A lysimeter experiment to investigate the leaching of veterinary antibiotics through a clay soil and comparison with field data. *Environ Pollut.* 2005;134(2):333-341. doi:10.1016/j.envpol.2004.07.021
- Koh S, Aoki T, Katayama Y, Takada J. Losses of elements in plant samples under the dry ashing process. *J Radioanal Nucl Chem.* 1999;239(3):591-594.
- Lalor GC, Onionwa PC, Vutchkov MK. Dry-ashing preconcentration for micro-reactor-based neutron activation of food and plant samples. *Int J Environ Anal Chem.* 2003;83(5):367-374.
- Landsberger S, George G, Lara R, Tamalis D, Louis Jean J, Dayman K. Analysis of Naturally Occurring Radioactive Material Using Neutron Activation Analysis and Passive Compton Suppression Gamma-Ray Spectrometry. *Nukleonika.* 2012;57:461-465.
- Lavergne S, Thompson JD, Garnier E, Debussche M. The biology and ecology of narrow endemic and widespread plants: A comparative

study of trait variation in 20 congeneric pairs. *Oikos*. 2004;107(3):505-518. doi:10.1111/j.0030-1299.2004.13423.x

Marple ML. Radium-226 in Vegetation and Substrates at Inactive Uranium Mill Sites. University of California. 1980.

Mendez MO, Maier RM. Phytostabilization of Mine Tailings in Arid and Semiarid Environments—An Emerging Remediation Technology. *Environ Health Perspect*. 2008;116(3):278-283. doi:10.1289/ehp.10608

Mishra T, Pandey VC. Phytoremediation of Red Mud Deposits Through Natural Succession. In: *Phytomanagement of Polluted Sites*. 2019:409-424. doi.org/10.1016/B978-0-12-813912-7.00016-8.

Nelson AW, May D, Knight AW, Eitrheim ES, Mehrhoff M, Shannon R, Schultz, MK. Matrix Complications in the Determination of Radium Levels in Hydraulic Fracturing Flowback Water from Marcellus Shale. *Environ Sci Technol Lett*. 2014; 1(5):204-208. doi:10.1021/ez5000379

Nirola R, Megharaj M, Palanisami T, Aryal R, Venkateswarlu K, Naidu R. Evaluation of metal uptake factors of native trees colonizing an abandoned copper mine – a quest for phytostabilization. *J Sustain Min*. 2015;14(3):115-123. doi:10.1016/j.jsm.2015.11.001

Padmavathiamma PK, Li LY. Phytoremediation technology: Hyper-accumulation metals in plants. *Water Air Soil Pollut*. 2007;184(1-4):105-126. doi:10.1007/s11270-007-9401-5

Pulhani V, Kayasth S, More AK. Determination of Traces of Uranium and

Thorium in Environmental Matrices by Neutron Activation Analysis. *J Radioanal Nucl Chem.* 2000;243:625-629.

doi:10.1023/A:1010693514287

Rumble MA, Bjugstad AJ. Uranium and radium concentrations in plants growing on uranium mill tailings in South Dakota. *Reclam Reveget Res.* 1986;4:271-277.

Ruth CE, Michel D, Hirschi M, Seneviratne SI. Comparative study of a long-established large weighing lysimeter and a state-of-the-art mini-lysimeter. *Vadose Zone J.* 2018;17(1).

Sam AK, Eriksson A. Radium-226 uptake by vegetation grown in Western Sudan. *J Environ Radioact.* 1995;29(1):27-38. doi:10.1016/0265-931x(95)90935-r

Singh S, Malhotra R, Bajwa B. Uranium uptake studies in some plants. *Radiat Meas.* 2005;40(2-6):666-669.  
doi:10.1016/j.radmeas.2005.01.013

Sorrentino J. Uranium Mine and Mill Workers are Dying, and Nobody Will Take Responsibility. *Workplace Fairness.* 2016. Available from: <https://www.workplacefairness.org/blog/2016/02/15/uranium-mine-and-mill-workers-are-dying-and-nobody-will-take-responsibility/>

Vandenhove H, Hees MV. Predicting radium availability and uptake from soil properties. *Chemosphere.* 2007;69(4):664-674.  
doi:10.1016/j.chemosphere.2007.02.

Vandenhove H, Olyslaegers G, Sanzharova N, Shubina O, Reed E, Shang Z,

Velasco H. Proposal for new best estimates of the soil-to-plant transfer factor of U, Th, Ra, Pb and Po. *J Environ Radioact.* 2009;100(9):721-732. doi:10.1016/j.jenvrad.2008.10.014

Zaidi JH, Arif M, Ahmad S, Fatima I, Qureshi IH. Determination of natural radioactivity in building materials used in the Rawalpindi/Islamabad area by  $\gamma$ -ray spectrometry and instrumental neutron activation analysis. *Appl Radiat Isot.* 1999;51(5):559-564. doi:10.1016/S0969-8043(99)00073-1

Zhang W, Cai Y, Tu C, Ma LQ. Arsenic speciation and distribution in an arsenic hyperaccumulating plant. *Sci Total Environ.* 2002;300:167-177.

Chapter 3:  
Growing Concerns:  
An Evaluation of ICRP Publications 108 and 136  
Via Analysis of Endemic Plants of the Southwest United States

Joshua Hargraves

Kathryn Higley

Nuclear Science and Engineering, Oregon State University

This manuscript has been submitted to Health Physics, May 2023.

## ABSTRACT

The International Commission on Radiological Protection (ICRP) has developed a framework for environmental radiological protection through Publications 108 and 136, which introduced the concept of Reference Animals and Plants (RAPs) and their respective dose coefficients. However, the applicability and accuracy of these guidelines in real-world scenarios have not been extensively explored. This study aims to critique the content of ICRP Publications 108 and 136 using in situ plant analyses of uptake from contaminated growth media. The assessment of the uptake of radionuclides by various plant species was done through laboratory experiments by growing plant species in contaminated soil and through field studies. The findings reveal that the actual dose rates for some plant species deviate significantly from those proposed in ICRP Publications 108 and 136, implying potential implications from the derived consideration reference levels (DCRLs) and overall radiological protection framework. The study highlights the intricacies of the need for refining the RAPs approach and dose coefficients based on in situ data to improve the accuracy and reliability of environmental radiological protection assessments.

### 3.1 INTRODUCTION

Environmental radiological protection has gained significant importance in recent years, primarily due to the increasing awareness of the potential effects of ionizing radiation on non-human biota and their habitats. The International Commission on Radiological Protection (ICRP) has made substantial efforts to develop a robust and scientifically grounded framework for assessing and mitigating the impact of ionizing radiation on the environment. ICRP Publications 108 and 136 serve as cornerstones of this framework, introducing the concept of Reference Animals and Plants (RAPs) and providing dose coefficients for these species.

ICRP Publication 108, titled "Environmental Protection - the Concept and Use of Reference Animals and Plants," establishes the rationale and selection criteria for RAPs, which include a diverse range of organisms such as mammals, birds, reptiles, amphibians, fish, arthropods, and vascular plants. The primary goal of using RAPs is to create a common basis for evaluating the potential effects of ionizing radiation on non-human biota, which can be applied consistently across different species and ecosystems (ICRP, 2008).

To assess the radiological impact on RAPs, the ICRP introduced the concept of Derived Consideration Reference Levels (DCRLs) in Publication 108. DCRLs serve as benchmarks for absorbed dose rates, which can be used to identify situations that warrant further investigation or may require protective actions. By comparing the calculated absorbed dose rates for RAPs

to the DCRLs, it becomes possible to evaluate the potential risks posed by ionizing radiation and make informed decisions regarding environmental protection measures.

Consequently, ICRP Publication 136 builds upon the foundation laid by Publication 108 by providing dose coefficients for the RAPs. Dose coefficients are essential for calculating absorbed dose rates for RAPs exposed to various radionuclides in their environments. The publication aims to establish a more consistent and reliable approach to assess the radiological impact on non-human biota and their habitats (ICRP, 2017).

While ICRP Publications 108 and 136 represent significant advancements in environmental radiological protection, the accuracy and applicability of their recommendations in real-world situations remain to be thoroughly investigated. In this paper, a critical evaluation of the content of these publications using in situ plant analyses of uptake from contaminated growth media is presented. The study aims to shed light on the potential discrepancies between the proposed RAPs approach, dose coefficients, and actual plant uptake rates in contaminated environments, ultimately highlighting the importance of refining the existing framework based on empirical in situ data.

## 3.2 METHODS

In order to evaluate the efficacy of the findings of ICRP Publications 108 and 136, an appropriate reference plant was chosen to compare the most similar morphological specimens for which in situ data existed. To this end, the Reference Grass was chosen as the nearest morphological specimen to the evaluated species of *Sporobolus airoides*, *Helianthus petiolaris*, *Kochia scoparia*, and *Atriplex canescens*.

### 3.2.1 The Reference Grass

In ICRP Publication 108, the reference grass is one of the 12 Reference Animals and Plants (RAPs) selected for the purpose of assessing the potential effects of ionizing radiation on non-human biota. The reference grass represents the category of vascular plants and provides a basis for evaluating radiation exposure to terrestrial plant communities.

The parameters used to model the reference grass in ICRP Publication 108 are based on a generic “Barley” grass species. The grass is modeled as an idealized ellipsoid with the following morphological parameters:

**Table 3.1.** The dimensions of an ellipsoid conforming to the spike of Reference Grass.

Reference Model	Major Axis (cm)	Minor Axis 1 (cm)	Minor Axis 2 (cm)
Grass Ellipsoid	5	1	1

The reference ellipsoid in Table 3.1 was modeled for external exposure to both an ‘effective’ planar source with a depth of 0.5 g cm<sup>-3</sup>, measured 1 m above the ground, and by a volume source in the top 10 cm of soil, again measured 1 m above the ground.

### 3.2.2 In Situ Species

A collection of the selected species for study, *Sporobolus airoides*, *Helianthus petiolaris*, *Kochia scoparia*, and *Atriplex canescens*, were acquired from a variety of commercial retailers. For soils, uranium laden soil was excavated from legacy mining sites with shovels from the surface to a maximum depth of 15 cm to capture the topsoil. The bulked soil sample was placed into thick contractor garbage bags inside of United States Shipping Grade plastic buckets, filling approximately three quarters of each bucket. The internal containment bags were securely closed with zip-ties. A maximum of 110 gallons (416 L) of soil was collected to meet UN 2910 Hazardous Shipper Restrictions. Shipping containers were inspected before leaving the site by swiping, at minimum, a 10 cm<sup>2</sup> area on the exterior of the container and analyzed with a scintillation counter in the on-site Environmental Restoration Group (ERG) office. Sample containers were driven from the field site near Grants, NM to the shipping facility in Albuquerque, NM, before being relocated to the Oregon State University (OSU) campus in Corvallis, OR. The containers were stored in the Oregon State University Radiation Center

(OSURC) at room temperature until use. Soils contained a variety of concentrations of uranium from 12 ppm to 199 ppm as measured by Instrumentalized Neutron Activation of Np-239. Two sites from this soil collection, A and B, represent the highest and lowest end of the uranium concentration spectrum in our soil media for test cases in this study.

For analysis of plant growth and translocation of contaminants, lysimeters were used. Greenhouse growth is not always a perfect representation of in situ scenarios, but with enough replicates of plants to sites a strong representation of natural uptake can be made (Gerzabek, 1998; Islam, 2011). Additionally, the high clay soils used in this scenario are particularly efficient when arranged in small scale lysimeter arrays (Kay, 2005; Ruth, 2018).

The study was conducted within a locked greenhouse enclosure at the OSURC in order to secure the radioactive soil. The greenhouse enclosure can house approximately five lysimeters per species (10 cm diameter x 25 cm height ABS pipe columns (~2.059 L)) filled approximately 80% with the contaminated soil, with the remaining space being filled with pea gravel and filter meshing to aid drainage) for 20 lysimeters total, an example of which can be seen in Figure 3.1. Water added to plants was conducted weekly at approximately 100 mL.

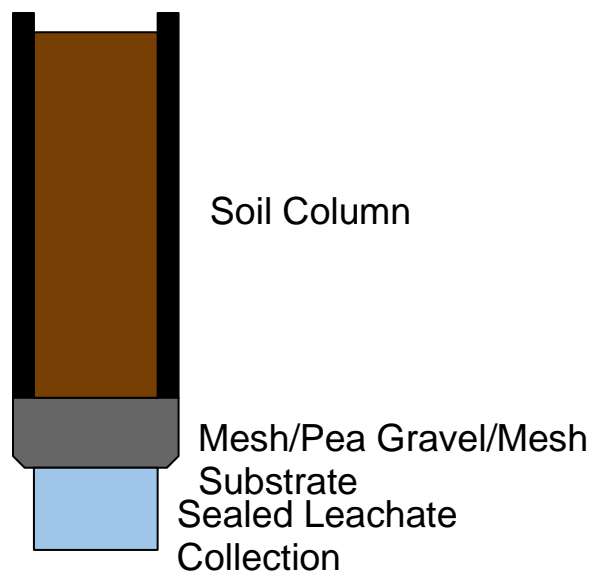


**Figure 3.1.(Rep. 2.2).** Example of lysimeter construction.

Bioconcentration factors (BCF) for the candidate plants were measured as concentration ratios of the relative fraction of contaminant radionuclides in the plant tissues to the respective levels in the soil media (Mishra, 2019; Zhang, 2002). For  $^{238}\text{U}$ , the ratio was measured by the concentrations determined through Neutron Activation Analysis of  $\text{Np-239}$  (Landsberger, 2012; Zaidi, 1999). For  $^{232}\text{Th}$ , the ratio was also measured by the concentrations determined through Neutron Activation Analysis, in this instance by  $^{233}\text{Pa}$  (Pulhani, 2000). Finally,  $^{226}\text{Ra}$  ratios were measured by the concentrations of the progeny of  $^{222}\text{Rn}$  after an ingrowth period via gamma spectroscopy (Jia, 2011; Nelson, 2014).

Using these transfer factors as a baseline, dose rate calculations were performed regarding the exposure scenarios outlined in ICRP 108 and 136 for comparative analysis. The dose rate in this case was calculated as the

partitioned amount of radionuclide in the soil media concentration respective to the geometry of the source material in ICRP 108 and 136 such that:

$$D_{rate, internal} = C_{medium} \times DCF_{internal}$$

Per ICRP 108 and 136, where  $C_{medium}$  represents the concentration of the contaminant in the source media, and the DCF is the dose correction factor tabulated from herb study calculations of idealized ellipsoids (ICRP, 2008; Tarenenko, 2004). The DCF for  $^{238}\text{U}$  internalized in grass is listed in table C.20 as  $5.8 \times 10^{-2} \text{ uGy day}^{-1}$  per  $\text{Bq kg}^{-1}$  in ICRP 108 or listed in table B.38 as  $2.5 \times 10^{-3} \text{ uGy hr}^{-1}$  per  $\text{Bq kg}^{-1}$  in ICRP 136, a difference of ~3% thus the ICRP 108 value was used for calculation. Likewise, for  $^{232}\text{Th}$ , the DCF was listed as  $5.5 \times 10^{-2} \text{ uGy day}^{-1}$  per  $\text{Bq kg}^{-1}$ , and for  $^{226}\text{Ra}$  the DCF was listed as  $3.4\text{E-}1 \text{ uGy day}^{-1}$  per  $\text{Bq kg}^{-1}$ . While ICRP 136 is a definitive improvement over the efforts of ICRP 108, the simplification to use of solely ICRP 108 data is for comparative purposes.

The BCF can adjust this calculation by modifying the  $C_{medium}$  by the amount additionally partitioned to the tissue such that a closer to in situ internal dose rate may be given by:

$$D_{rate, internal, adjusted} = ((BCF \times C_{medium}) + C_{medium}) \times DCF_{internal}$$

### 3.3 RESULTS & DISCUSSION

Astute observation may indicate that while *Sporobolus airoides* may be a grass, *Helianthus petiolaris*, *Kochia scoparia*, and *Atriplex canescens* are definitely not barley, wheat, or rye variants. However, in lack of appropriate reference plants, the grass is the most morphologically similar organism, and was modeled in ICRP 108 and 136 in the most similar means to traditional terrestrial growth scenarios. Using the model grass as a reference point, the internal dose rates for each plant and for three contaminants (Radium-226, Thorium-232, and Uranium-238) were assembled. While mathematically obvious, there will generally be an ‘artificial’ increase in the internal dose rate for all examples, but the differences between these increases between plants and between sites should be recognized.

Generally, nature is not confined to homogeneous infinite planes with structural densities in common with that of ICRU four component tissues. Soil chemistry and physical characteristics perform in a myriad of ways for the translocation of any particular element or substance, especially for radionuclides. Radium can chemically behave as calcium, which has many implications for biological uptake in living plants, as well as bindings in the organic matter of soil. Thorium translocates predominantly at pH of 6.5, but other factors show no overwhelming statistical significance and may depend

on the specificity of components of the site (IAEA, 2009; IAEA, 2010; Mitchell, 2013). Uranium is similar in its particular dependence on pH to translocate to the tissues of plants, but also shares a dependence on the variation of clay content, and iron presence alongside organic matter (EPA, 1999; IAEA, 2009; IAEA, 2010). Cumulatively, these considerations must be acknowledged as sources of potential discontinuity with what ICRP 108 and 136 have prescribed for dose rates and what any adjustments may make. With this caveat, adjusted dose rates should be evaluated as an example of the inability to accurately describe the processes of dose within situ plant tissues using only the geometrically and volumetrically simplified RAPs.

### 3.3.1 Uranium Comparisons

**Table 3.2.** Estimated internal dose rates in plant tissues from  $^{238}\text{U}$  laden media using the dose rate equation in ICRP 108 and the results of dose per calculated bioconcentration factors. Blank spaces denote values below detectable limits.

Plant Species	BCF for growth in Site A 144 Bq kg <sup>-1</sup> 238U Soil	Internal Dose Rate per ICRP 108 and 136 (uGy day <sup>-1</sup> )	Internal Dose Rate adjusted per BCF (uGy day <sup>-1</sup> )	BCF for growth in Site B 2470 Bq kg <sup>-1</sup> 238U Soil	Internal Dose Rate per ICRP 108 and 136 (uGy day <sup>-1</sup> )	Internal Dose Rate adjusted per BCF (uGy day <sup>-1</sup> )
<i>Sporobolus airoides</i>	0.58	8.35	13.20	0.46	143.26	209.16
<i>Helianthus petiolaris</i>	3.47	8.35	37.33	0.46	143.26	209.16
<i>Kochia scoparia</i>	0.59	8.35	13.28	0.41	143.26	202.0
<i>Atriplex canescens</i>	1.16	8.35	18.04	-	143.26	143.26

Table 3.2 highlights the overall increase in uptake at the lower end of the uranium concentration spectrum in the soil of *Helianthus petiolaris* with an increased internal dose rate of 347%, the rate postulated by ICRP 108 and 136. Likewise, the *Atriplex canescens* experiences an increased internal dose rate of 116%. *Sporobolus airoides* and *Kochia scoparia* saw relatively moderate increases at 58% and 59%, respectively.

At the relatively higher end of uranium concentration, the dose rate increases are more moderate. Both *Sporobolus airoides* and *Helianthus petiolaris* experience an increase of 46%. Similarly, *Kochia scoparia* experiences an increase of 41%. Since the samples of *Atriplex canescens* grown in Site B soils did not mature enough in growth to get a sample that could meet detection limits, there was no discernible difference for the purposes of this study.

### 3.3.2 Thorium Comparisons

**Table 3.3** Estimated internal dose rates in plant tissues from  $^{232}\text{Th}$  laden media using the dose rate equation in ICRP 108 and the results of dose per calculated bioconcentration factors. Blank spaces denote values below detectable limits.

Plant Species	BCF for growth in Site A 52 Bq kg <sup>-1</sup> 232Th Soil	Internal Dose Rate per ICRP 108 and 136 (uGy day <sup>-1</sup> )	Internal Dose Rate adjusted per BCF (uGy day <sup>-1</sup> )	BCF for growth in Site B 48 Bq kg <sup>-1</sup> 232Th Soil	Internal Dose Rate per ICRP 108 and 136 (uGy day <sup>-1</sup> )	Internal Dose Rate adjusted per BCF (uGy day <sup>-1</sup> )
<i>Sporobolus airoides</i>	0.37	2.86	3.92	1.03	2.64	5.36
<i>Helianthus petiolaris</i>	2.17	2.86	9.07	0.10	2.64	2.90
<i>Kochia scoparia</i>	0.11	2.86	3.17	0.19	2.64	3.14
<i>Atriplex canescens</i>	0.14	2.86	3.26	-	2.64	2.64

Table 3.3 describes the modest increase in uptake, with a relatively much higher uptake in *Helianthus petiolaris* at the higher end of  $^{232}\text{Th}$  concentration in the soil medium. Though the difference between these concentrations is small (8%), the impact on uptake is quite a bit larger.

For *Sporobolus airoides* growth in  $52 \text{ Bq kg}^{-1} \text{ }^{232}\text{Th}$  soil, there is a 37% increase in the internal dose rate. Comparatively, for growth in  $48 \text{ Bq kg}^{-1} \text{ }^{232}\text{Th}$  soil, there is a 103% increase. *Helianthus petiolaris* grown in  $52 \text{ Bq kg}^{-1} \text{ }^{232}\text{Th}$  soil yields a 217% increase and in  $48 \text{ Bq kg}^{-1} \text{ }^{232}\text{Th}$  soil it is a 10% increase. *Kochia scoparia* when grown in  $52 \text{ Bq kg}^{-1} \text{ }^{232}\text{Th}$  soil sees 11% increase, and growth in  $48 \text{ Bq kg}^{-1} \text{ }^{232}\text{Th}$  soil lends to a 19% increase. Finally, *Atriplex canescens* sees a 14% increase in internal dose rate in  $52 \text{ Bq kg}^{-1} \text{ }^{232}\text{Th}$  soil, but again as no samples met the limit for detection grown in Site B soil the dose rate is the same as postulated by ICRP 108 and 136 for the purposes of this comparison.

### 3.3.3 Radium Comparisons

**Table 3.4.** Estimated internal dose rates in plant tissues from <sup>226</sup>Ra laden media using the dose rate equation in ICRP 108 and the results of dose per calculated bioconcentration factors. Blank spaces denote values below detectable limits.

Plant Species	BCF for growth in Site A 22 Bq kg <sup>-1</sup> 226Ra Soil	Internal Dose Rate per ICRP 108 and 136 (uGy day <sup>-1</sup> )	Internal Dose Rate adjusted per BCF (uGy day <sup>-1</sup> )	BCF for growth in Site B 409 Bq kg <sup>-1</sup> 226Ra Soil	Internal Dose Rate per ICRP 108 and 136 (uGy day <sup>-1</sup> )	Internal Dose Rate adjusted per BCF (uGy day <sup>-1</sup> )
<i>Sporobolus airoides</i>	3.46	7.48	33.36	0.57	139.06	218.32
<i>Helianthus petiolaris</i>	2.69	7.48	27.60	0.42	139.06	197.47
<i>Kochia scoparia</i>	2.40	7.48	25.43	1.07	139.06	287.85
<i>Atriplex canescens</i>	1.41	7.48	18.03	0.10	139.06	152.97

Table 3.4 covers the results for Radium-226. The lower concentration gradient of Site A, *Sporobolus airoides* sees the highest internal dose rate increase with the adjustment at 346% of the value of the reference internal dose rate.

*Helianthus petiolaris* and *Kochia scoparia* see a relatively similar increase in dose rate at 269% and 240%, respectively. *Atriplex canescens* sees the smallest increase at 141%.

For Site B, the increases are still present but more statistically muted. *Sporobolus airoides* and *Helianthus petiolaris* see increases of 57% and 42%, whereas *Kochia scoparia* observes an increase of 107%. *Atriplex canescens* once more sees the smallest increase at 10%.

### 3.3.4 Derived Consideration Reference Levels

By combining the adjusted dose rates tabulated prior with those calculated for the external exposure scenarios, a total absorbed dose to each studied plant group can be calculated.

**Table 3.5.** Comparison of the total dose rates calculated as the sum of the internal and external dose rates for all radionuclides of concern, differentiated by Site and method of calculation.

Plant Species	Total Dose Rate at Site A per ICRP 108/136 (uGy day <sup>-1</sup> )	Total Dose Rate at Site A with adjustment (uGy day <sup>-1</sup> )	Total Dose Rate at Site B per ICRP 108/136 (uGy day <sup>-1</sup> )	Total Dose Rate at Site B with adjustment (uGy day <sup>-1</sup> )
<i>Sporobolus airoides</i>	18.87	50.65	288.24	436.12
<i>Helianthus petiolaris</i>	18.87	74.18	288.24	412.81
<i>Kochia scoparia</i>	18.87	42.06	288.24	496.27
<i>Atriplex canescens</i>	18.87	39.50	288.24	302.14

Comparing the results of Table 3.5 with the DCRLs outlined in table 6.4 of ICRP Publication 108, all values fall within the non-shaded region considered as a level at which further evaluation should be warranted. Regrettably, little literature exists studying any of these plants in depth regarding radiation dose or dose effects, leaving only this paper as a first analysis of dose to any of these particular plants.

While again none of these plants experienced a bracket change in the DCRL table, all species at Site A experienced a higher dose rate greater than 100% of the estimated value, with *Helianthus petiolaris* experiencing the greatest change at 293%. At Site B, the effect is far more muted, with *Kochia scoparia* having the highest change at 72% increase relative to the ICRP findings, *Sporobolus airoides* at a 51% increase, and *Helianthus petiolaris* seeing a 43% increase, relative to ICRP findings. For *Atriplex canescens* the only variation was in the radium section for adjustments, leading to a modest 4% increase in dose rate. It is uncertain what condition prevented growth of this species at Site B in greenhouse study as the species is prolific at the location the soil was extracted.

### 3.4 CONCLUSION

Through a comprehensive analysis of in situ plant uptake from contaminated growth media, there were significant deviations in the actual dose rates of some plant species compared to the proposed values in the ICRP guidelines.

These discrepancies emphasize the need for refining the RAPs approach and dose coefficients based on in situ data to improve the accuracy and reliability of environmental radiological protection assessments.

The results also highlight the complex interplay between radionuclide uptake and various soil characteristics. These factors contribute to potential discontinuity between the ICRP recommendations and actual dose rates, and thus warrant further investigation to develop a more accurate and site-specific radiological protection framework.

The derived consideration reference levels (DCRLs) should be cautiously interpreted, as the observed and appropriately adjusted internal dose rates for several plant species place the dose rates significantly upward, nearing the range that necessitates further evaluation. This underscores the importance of refining and validating the existing RAPs approach to ensure that environmental radiological protection assessments are both reliable and robust.

### 3.5 ACKNOWLEDGEMENTS

Dr. Kathryn Higley for her invaluable insight in extraction and methodology of study for radioecological work.

## REFERENCES

- EPA. Understanding variation in partition coefficient Kd values Volume II: Review of Geochemistry and Available Kd values for Cadmium, Cesium, Chromium, Lead, Plutonium, Radon, Strontium, Thorium, Tritium (3H), and Uranium US Environmental Protection Agency Report. US EPA. 1999. 402-R-99-004B (Washington, DC:EPA)
- Gerzabek MH, Strebl F, Temmel B. Plant uptake of radionuclides in lysimeter experiments. *Environmental Pollution*, 99(1), 93-103. 1998.
- IAEA. Quantification of Radionuclide Transfer in Terrestrial and Freshwater Environments for Radiological Assessments. IAEA-TECDOC-1616. 2009. (Vienna: International Atomic Energy Agency)
- IAEA. Handbook of Parameter Values for the Prediction of Radionuclide Transfer in Terrestrial and Freshwater Environments IAEA Technical Report Series No. 472. 2010. (Vienna: International Atomic Energy Agency)
- ICRP. Environmental Protection - the Concept and Use of Reference Animals and Plants. ICRP Publication 108. *Ann ICRP*. 2008;38(4-6).
- ICRP. Dose coefficients for nonhuman biota environmentally exposed to radiation. ICRP Publication 136. *Ann ICRP*. 2017;46(2).
- Islam M, Mao S, M Shahidul Alam A, Eneji A, Hu Y, Xue X. A Lysimeter Study for Leaching Losses, Sustainable Fertilization, and Growth Responses of Corn (*Zea mays* L.) Following Soil Amendment with a

Water-Saving Superabsorbent Polymer. *Applied Engineering in Agriculture*. 27. 757-764. 2011. doi:10.13031/2013.39575

Jia G, Jia J. Determination of radium isotopes in environmental samples by gamma spectrometry, liquid scintillation counting and alpha spectrometry: A review of analytical methodology. *J Environ Radioact*. 2012;106:98-119. doi:10.1016/j.jenvrad.2011.12.003

Kay P, Blackwell PA, Boxall, AB. A lysimeter experiment to investigate the leaching of veterinary antibiotics through a clay soil and comparison with field data. *Environmental Pollution*, 134(2), 333-341. 2005. doi:10.1016/j.envpol.2004.07.021

Landsberger S, George G, Lara R, Tamalis D, Louis Jean J, Dayman K. Analysis of Naturally Occurring Radioactive Material Using Neutron Activation Analysis and Passive Compton Suppression Gamma-Ray Spectrometry. *Nukleonika*. 2012;57:461-465.

Mitchell, N & Perez-Sanchez, Danyl & Thorne, Michael. A review of the behaviour of U-238 series radionuclides in soils and plants. *Journal of radiological protection : official journal of the Society for Radiological Protection*. 2013. 33. R17-R48. 10.1088/0952-4746/33/2/R17.

Mishra T, Pandey VC. Phytoremediation of Red Mud Deposits Through Natural Succession. In: *Phytomanagement of Polluted Sites*. 2019:409-424. doi.org/10.1016/B978-0-12-813912-7.00016-8.

Nelson AW, May D, Knight AW, Eitrheim ES, Mehrhoff M, Shannon R, Schultz, MK. Matrix Complications in the Determination of Radium

Levels in Hydraulic Fracturing Flowback Water from Marcellus Shale.

Environ Sci Technol Lett. 2014; 1(5):204-208. doi:10.1021/ez5000379

Pulhani V, Kayasth S, More AK. Determination of Traces of Uranium and Thorium in Environmental Matrices by Neutron Activation Analysis. J Radioanal Nucl Chem. 2000;243:625-629. doi:10.1023/A:1010693514287

Ruth CE, Michel D, Hirschi M, Seneviratne, SI. Comparative study of a long-established large weighing lysimeter and a state-of-the-art mini-lysimeter. Vadose Zone Journal, 17(1). 2018.

Taranenko V, Prohl G, Go´mez-Ros JM. Absorbed dose rate conversion coefficients for reference biota for external photon and internal exposures. J. Radiol. Prot. 24, A35–A62. 2004.

Zaidi JH, Arif M, Ahmad S, Fatima I, Qureshi IH. Determination of natural radioactivity in building materials used in the Rawalpindi/Islamabad area by  $\gamma$ -ray spectrometry and instrumental neutron activation analysis. Appl Radiat Isot. 1999;51(5):559-564. doi:10.1016/S0969-8043(99)00073-1

Zhang W, Cai Y, Tu C, Ma LQ. Arsenic speciation and distribution in an arsenic hyperaccumulating plant. Sci Total Environ. 2002;300:167-177.

Chapter 4:  
Banana For Scale:  
An Analysis of Voxelized Phantoms of the Banana for use in  
Dosimetric Modeling

Joshua Hargraves<sup>1</sup>

Delvan Neville<sup>2</sup>

Kathryn Higley<sup>1</sup>

<sup>1</sup>Nuclear Science and Engineering, Oregon State University

<sup>2</sup>Sun Nuclear Corporation

## ABSTRACT

The ICRP has provided simplified phantoms for estimating radiological dose from external and internal sources of radiation; however, there are circumstances when highly accurate calculation of absorbed dose may be more useful. The use of anatomically accurate phantoms may provide insight into exposure scenarios. The process uses a collection of CT and/or MRI images, delineates organ structures within each image slice, and then prepares a volumetric phantom. This phantom is coupled with a radiation transport code (e.g., GEANT4 10.5) to assess the extent of radiation transmission and energy absorption through tissues of interest. Precise dosimetric phantoms have been challenging to generate due to their extensive use of time and need for proprietary software. An effort was made to develop open-source software to provide the missing link between image collection and radiation transport calculation. The software, FSOPhantom (Faster, Sharper and Open), works with modified Geant4 release version 10.5 and is coupled with the open-source medical image analysis software 3D Slicer. FSOPhantom allows for import of triangular mesh geometry produced from STL (STereo Lithograph) files before coupling them to particle tracking software. These very fine scale geometric structures can be represented by hundreds of thousands of small triangles, even if the rest of the model consists of fewer, much larger triangles. This program was used to generate a new phantom dosimetric model for a

previously unstudied, yet infamous among the radiation professional community, terrestrial plant, the common banana (*Musa acuminata Colla*).

## 4.1 INTRODUCTION

Internal dosimetry has historically been the science of understanding how internalized sources of ionizing radiation impacts tissues within an organism. While many studies have been done to measure these effects, primarily in humans, prospective studies have made use of novel features through computer simulated models. The history of these models originates from medical practice, particularly the use of tracer studies in the late 1920s.

However, it was not until Marinelli modeled a patient's tissues as a cylindrical volume that the first model was born. From there, the models grew into individualized spheres for each respective organ in the human body as demonstrated by Quimby (Xu, 2014). The 1960s further developed these approximations through the use of the most powerful tool now in use: the computer. Ellett was the first to publish computer generated energy depositions based on rudimentary phantom shapes, utilizing Monte Carlo approximations to determine the path of gamma rays as they passed through a medium. This culminated in perhaps the most widely known modeling program for internal dosimetry, Monte Carlo N-Particle, or MCNP, in 1977 via Los Alamos National Laboratory. However, all of this work was still in the realm of modeling a human being.

Models have long been a mainstay of estimating dose and exposure scenarios, especially in the case of non-human biota. However, modern models make use of ellipsoids or similar geometric shapes with infinitely homogeneous structures of particular density (ICRP, 2008; ICRP 2017). Novel methods of creating phantom voxel models of organisms, such as those developed by Neville (2019), allow for a more accurate portrayal of biota for particular relative absorbed fraction parameters in tissue and organs. Incidentally, such phantom models show some discrepancies with established literature (Condon, 2019; Ruedig, 2015).

ICRP 108 and 136, in particular reference “Reference Animal and Plant” (RAP) considerations for non-human biota, including small terrestrial plants, such as the common grass, to large terrestrial plants, such as the Scots Pine. To this date, a very small number of specific voxelized phantoms have been created for these RAPs and even fewer have been for the plants outlined (Biermans, 2014; Condon, 2019; Yoschenko, 2011). Functioning as key endemic organisms of world ecosystems, further consideration towards the complexities of these non-human organisms would be ideal as only one terrestrial plant model has been constructed and cross-analyzed between phantom structures (Montgomery, 2020).

Within this paper are the first dosimetric models of the banana (*Musa acuminata Colla*), a traditional food of the Philippines that has spread to much of the world, to become a staple crop of the world’s fruit supply in the modern era (Langdon, 1993). The banana fruit is one of the most commonly used

references for equivalent dose communication, as seen in the commonly touted “Banana Equivalent Dose” (Mansfield, 1995).

## 4.2 METHODS

### 4.2.1 Voxel Overview

A voxel model is a three-dimensional digital representation of an object or space made up of voxels, which are volumetric pixels. Voxel models are created through a process called voxelization, where a mesh or point cloud is converted into a voxel grid. This grid can then be manipulated to simulate various scenarios or analyze different properties of the object or space.

The creation of a voxel model involves several steps, including data acquisition, preprocessing, voxelization, and postprocessing. Data acquisition involves obtaining data about the object or space using techniques such as computerized tomography (CT) scanning, magnetic resonance imaging (MRI), or laser scanning. Preprocessing involves cleaning and preparing the data for voxelization, while voxelization involves converting the data into a voxel grid. Postprocessing, such as the case of FSOPhantom, involves analyzing the voxel model and extracting relevant information from it.

While voxel models can be useful for simulating and analyzing various scenarios, they also have several limitations compared to in situ analysis. For example, voxel models are based on discrete representations of objects or

spaces and may not capture all of the complexities and nuances of the real world. Additionally, voxel models may not accurately represent physical processes or phenomena, and their accuracy may be limited by factors such as voxel size and resolution. Finally, voxel models may not be able to account for certain types of interactions or behaviors that can only be observed through in situ analysis.

#### 4.2.2 Computational Modeling Programs

A novel program developed at Oregon State University was used to generate dosimetric modeling of *M. acuminata* Colla used triangular mesh recreations of MRI or CT scanned organisms. This program, Faster, Sharper Open Phantom (FSOPhantom) was developed by Dr. Delvan Neville and consists of a customized fork of GEometry ANd Tracking 4 (GEANT4), which interfaces with 3DSlicer to provide an open-source method for dosimetric modeling and deconstruction.

3D Slicer is a powerful, open-source software package developed by the National Institutes of Health (NIH) for medical image analysis, visualization, and research. It is a versatile tool that allows users to process and analyze medical image data, including MRI, CT, and PET scans, in three dimensions.

One of the key features of 3D Slicer is its user-friendly interface, which makes it easy for medical professionals and researchers to manipulate

and analyze large datasets. The software offers a range of sophisticated tools for image segmentation, registration, and fusion, as well as advanced algorithms for volume rendering and image-based modeling (Fedorov, 2012).

GEANT4 is a toolkit for the simulation of the passage of particles through matter. It is used extensively in the fields of high energy physics, nuclear physics, space science, medical physics, and radiation protection. GEANT4 was developed in 1993 by CERN, the European Organization for Nuclear Research, and its collaborators.

The code GEANT4 allows users to define the geometry of their experimental setups, specify the particles to be simulated, and select the physics processes to be included in the simulation. GEANT4 uses Monte Carlo techniques to simulate the passage of particles through matter, tracking each particle's position, energy, and other properties as it interacts with the material (Agostinelli, 2003; Allison, 2006, 2016).

GEANT4 includes a large number of models for electromagnetic, hadronic, and optical interactions, and has been extensively validated against experimental data. It can simulate a wide range of particle types, energies, and geometries, from subatomic particles to cosmic rays and astrophysical phenomena. It is open-source software, so users can modify the code or develop their own models and share them with the community.

However, one of the limitations of GEANT4 is that it can be computationally intensive, especially for complex geometries or high-energy particles. This can require significant computing resources and long

simulation times. Additionally, the accuracy of the simulation results depends on the quality of the input data and the models used, so careful validation and verification of the simulations is important (Agostinelli, 2003; Allison, 2006, 2016). This limitation extends to FSOPhantom, where for large numbers of vertices and triangles loading time may be longer than is feasibly desired.

Finally, for repair of mesh errors and to reduce file sizes and triangles and vertices by orders of magnitude, Meshmixer was utilized. Meshmixer is a state-of-the-art and free tool for analyzing and mixing meshes of triangular polygons in medical, physical engineering, or public sector projects (Autodesk, 2018).

#### 4.2.3 Post MRI Modelling of Plant Tissues

3DSlicer was used to develop the MRI scans of *M. acuminata Colla* into a three-dimensional object with segmentation of individual structures within the fruit that serve variable organic functions. The model banana provided by Boston University Medical School was prepared via a Philips Intera/Achieva 3T MRI Machine, using Proton Density Weighting. The banana was segmented into two models: a uniform banana consisting of homogenous tissue throughout and a more detailed model (Figure 4.1) consisting of a ~3 mm thick skin or epicarp, internalized “meat” or mesocarp, and the placenta, loculus, and endocarp as a combined third segment dubbed the “Internals” due to resolution constraints.

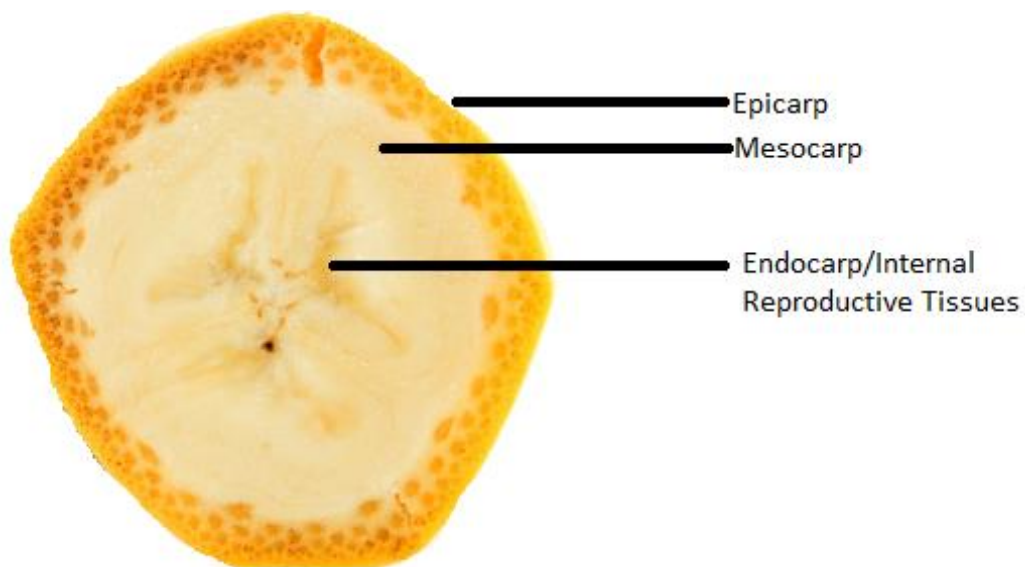


**Figure 4.1.** Biological Drawing of a Cross Section of a Banana.

Segments of the banana were analyzed by alternating contrast levels and labeled through use of the Paint, Hollow, and Level Trace tools manually, as seen in Figure 4.2. These segments were exported as binary STL files at roughly 300 MB each. However, the number of triangles and vertices was overabundant for practical purposes, as well as the presence of step level edge anomalies due to the limitations of scan slices along the coronal plane.

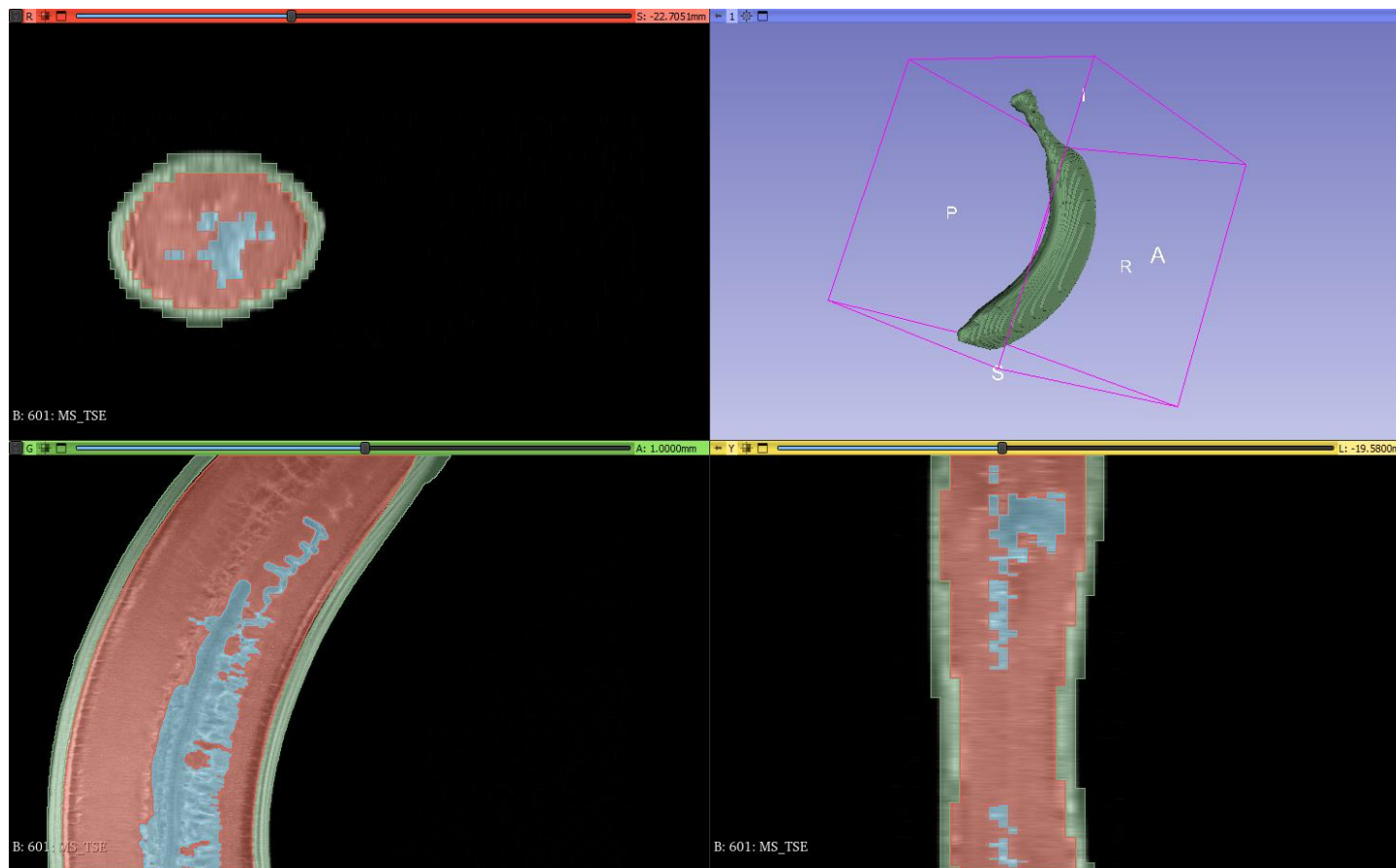


**Figure 4.2.** Example of a first pass of segmentation in 3DSlicer, highlighting the colloquial skin, flesh, and central reproductive structure as separate structures.

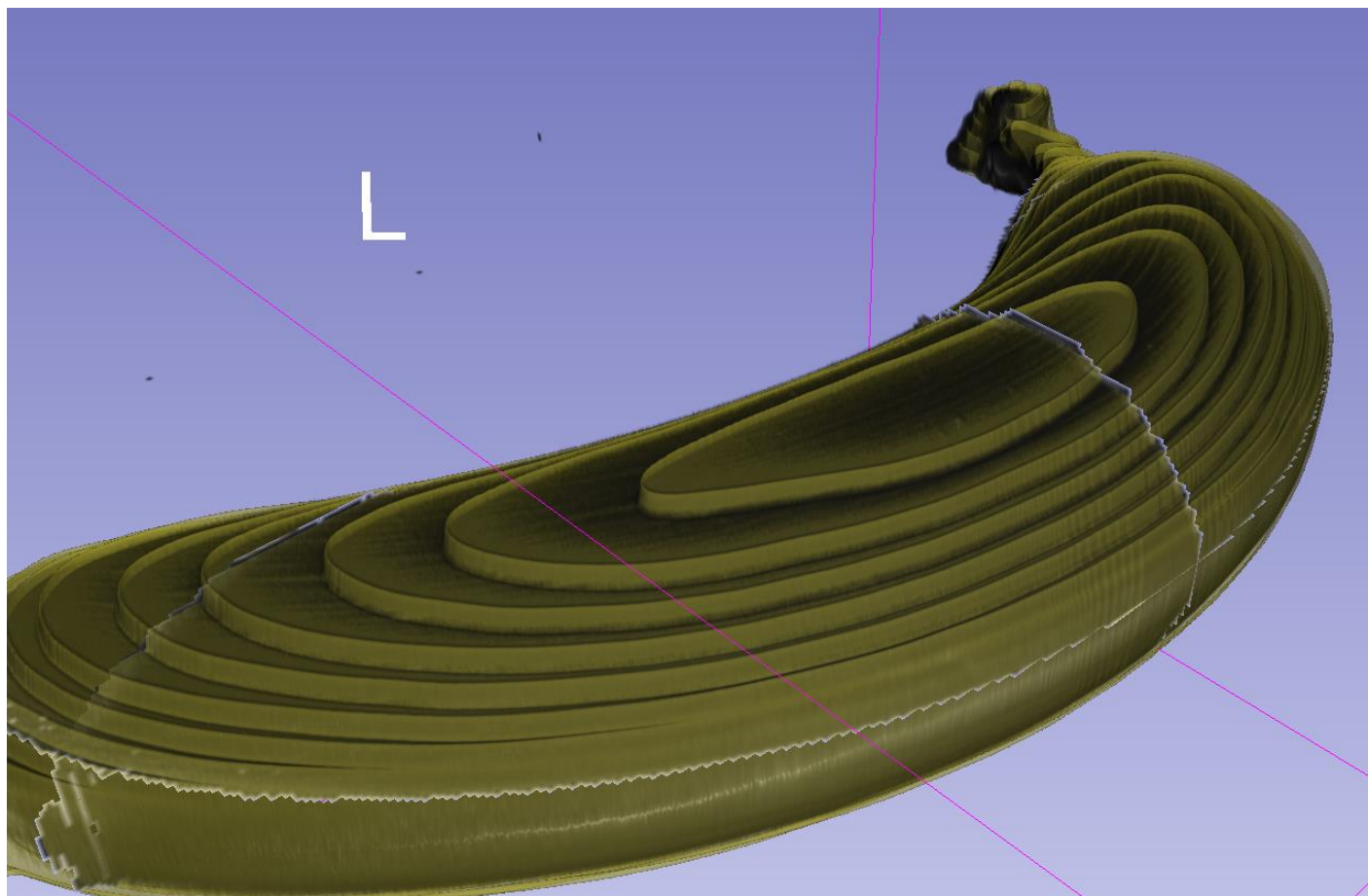


**Figure 4.3:** Example of “step” anomalies in segmentation of a volume due to a limitation in slices along a plane.

In the case of these anomalies seen in Figure 4.3, the STL files were run through a commercial tool for repairing 3D models, Meshmixer. However, any similar tool that has both a smoothing and a decimation feature can be used with equal effect. Using these utilities, the models were reduced to at most 11540 KB while preserving the geometry of the samples.

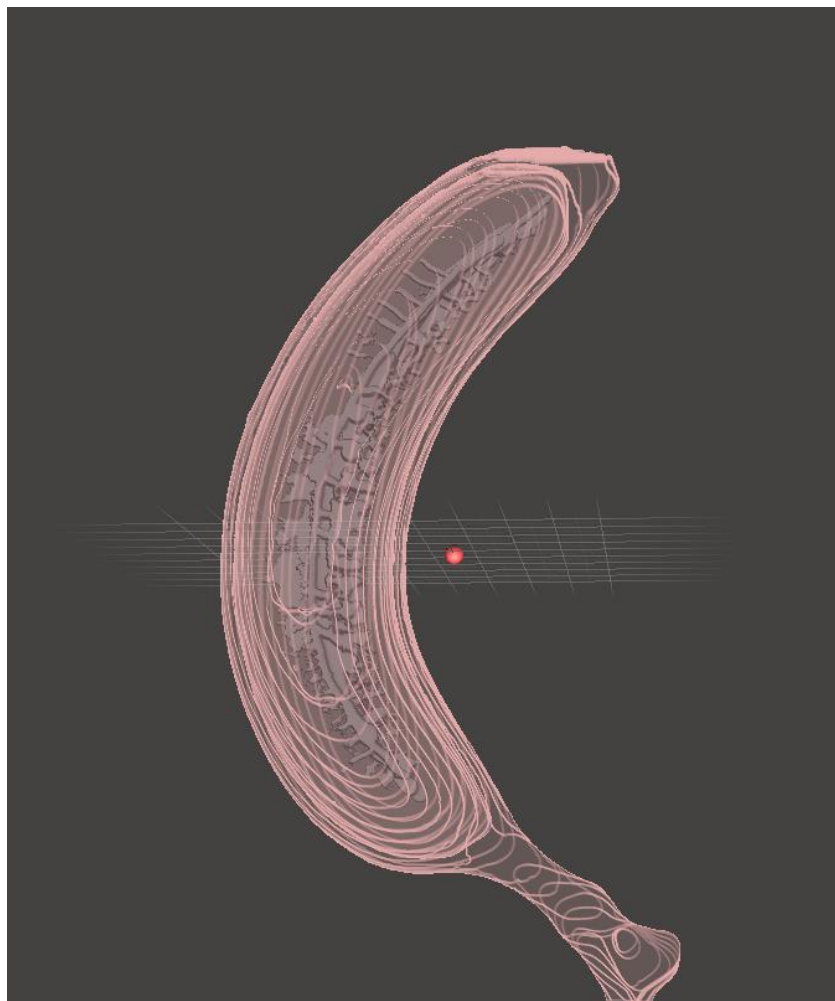


**Figure 4.4.** Semi-smoothed meshes preserving geometry of the internal meat and reproductive network overlaid across each other in Meshmixer.

The dimensions of the final meshes approximated to the nearest rectangular prism were as follows:

**Table 4.1.** Dimensions of the various segments generated as STL meshes for study in FSOPhantom.

Tissue Section	Max Length (mm)	Max Width (mm)	Max Height (mm)
Epicarp	200	43	104
Mesocarp	164	31	78
Internals	145	17	68

The results of which can be seen in Figure 4.4 as a nested phantom structure respecting the geometry of each subsequent segment. Note that each segment is exported as a mesh, meaning that each is deemed as a hollow structure until filled by an appropriate application.

#### 4.2.4 Generating a “Reference” Banana

Neither ICRP Publication 108 nor 136 intended to address nonhuman biota have covered fruits at this time, however a phantom ellipsoid generated in the same style as these endeavors can be obtained. Using Meshmixer, an ellipsoid of dimensions similar to the epicarp’s nearest rectangular prism was generated as seen in Figure 4.5.

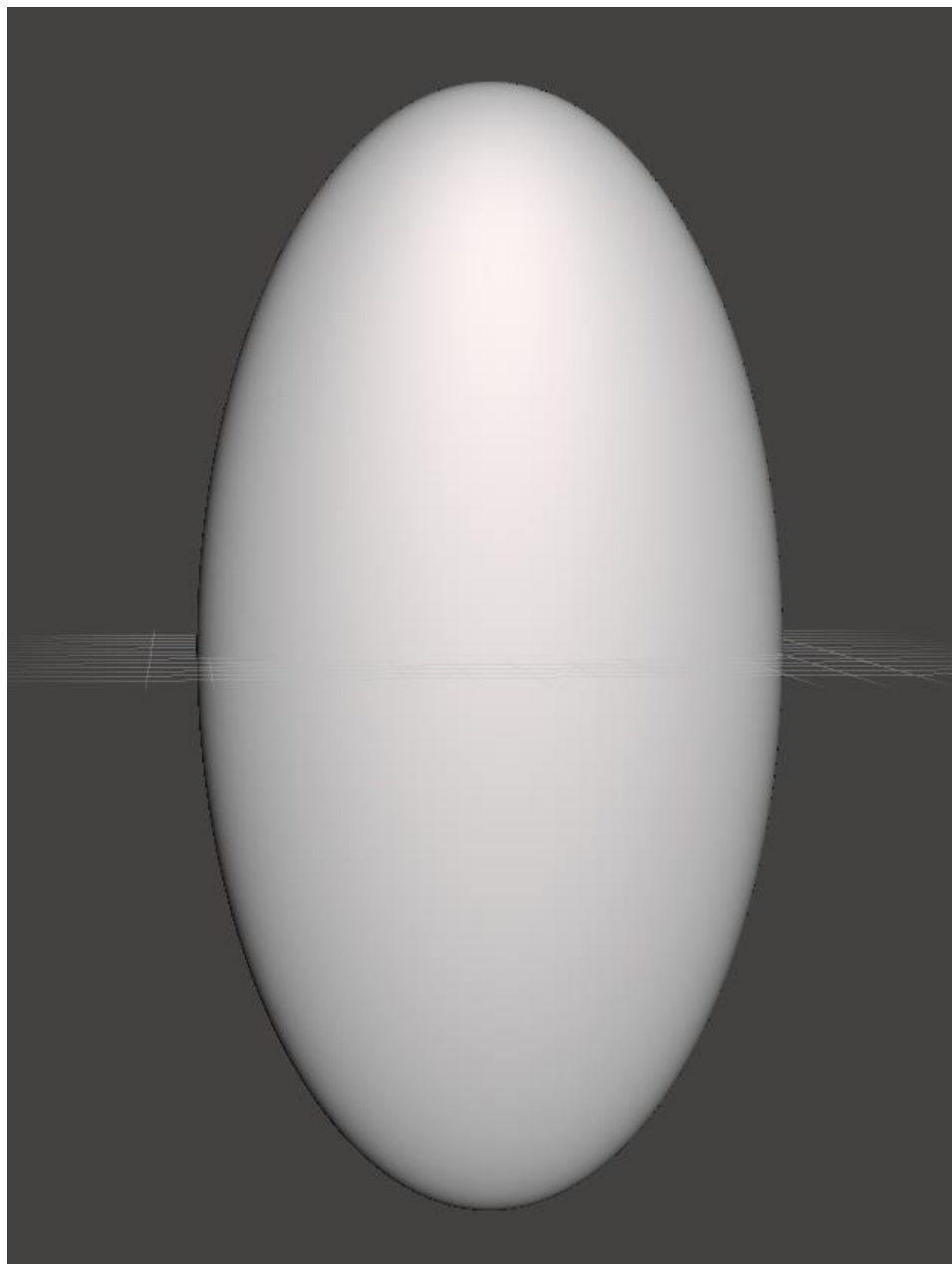


**Figure 4.5.** An ellipsoidal model of a “Reference” Banana conforming to the idealized dimensions of the nearest rectangular prism from a scan of a real banana.

**Table 4.2.** The dimensions of an ellipsoid conforming to the nearest rectangular prism from a scan of a real banana, for use as a “Reference” Banana.

Model Reference	Major Axis (mm)	Minor Axis 1 (mm)	Minor Axis 2 (mm)
Banana Ellipsoid	200	43	104

#### 4.2.5 FSOPhantom Specifications

FSOPhantom relies on the provision of material definition files (MDEF) for each STL loaded as well as a MDEF for the surrounding medium. These files are simple text files formatted to contain the material name as a “single word (no spaces), space, the material density in  $\text{g cm}^{-3}$ , space, and the number of elements that comprise the material. Lines 2 and beyond give the symbol for an element, space, then the weight fraction for that element” (Neville, 2020). For comparison between models ellipsoidal in nature and the whole banana, the former was given a material definition of International Commission on Radiation Units and Measurements (ICRU) 4-component tissue (ICRP, 2010).

For the more thorough modeling of the biologically accurate segmentations, each particular segment’s density and weight fraction per element was calculated based on the average mass of respective constituent tissues (Soltani, 2011) relative to the volume calculated per voxel in Meshmixer/3DSlicer and elemental compositional analyses of related species (Anhwange, 2009; Pereira, 2021).

**Table 4.3.** The material density of the various segments of the banana component tissues alongside the elemental compositions of each, including C, O, N, H, Cl, K, Mn, Fe, Cu, Zn, Br, Rb, Sr in the Epicarp, with the loss of Ca in the Mesocarp, and ICRU material for the internal combination.

Tissue Section	Material Density (g cm <sup>-3</sup> )	Elemental Weighting Fractions
Epicarp	0.86	14
Mesocarp	0.66	13
Internals	0.66	4

Combined, this yields a phantom banana with an approximate mass of 156 g when combining all constituent models, or individually a 9 g internals, 81 g mesocarp, and a 66 g epicarp.

### 4.3 RESULTS

All models were run through FSOPhantom in an envelope of air (0.0012 g cm<sup>-3</sup> and six elemental weighting fractions) exceeding the model geometry out to ten times the initial envelope containing only the host model geometry to ensure that appropriate particle backscattering could occur when relevant. Following the work of prior authors (Caffrey, 2016; Condon, 2019; Neville, 2020), a similar range of gamma energies were simulated: 0.01, 0.015, 0.02, 0.03, 0.05, 0.1, 0.2, 0.4, 0.5, 0.7, 1.0, 1.5, 2.0 and 4.0 MeV, and the electron energies simulated were 0.01, 0.015, 0.02, 0.03, 0.05, 0.1, 0.2, 0.4, 0.5, 0.7, 1.0, 1.5, 2.0, 4.0 MeV. Due to the limits of time, efficiency, and ability, 50,000 histories were run for each simulated energy. All sources were generated as a volumetric parallelepiped.

### 4.3.1 Ellipsoidal Reference Model

**Table 4.4a.** The output of running FSOPhantom over an idealized reference banana phantom, consisting of ICRU 4 Tissue for gamma sources.

Particle	Energy (keV)	Ellipsoid Mean Dose (pGy)	Absorbed Fraction	Mean Dose Fractional Standard Deviation
gamma	10	$3.27 \times 10^{-3}$	$9.55 \times 10^{-1}$	$9.67 \times 10^{-4}$
gamma	15	$4.34 \times 10^{-3}$	$8.45 \times 10^{-1}$	$1.91 \times 10^{-3}$
gamma	20	$4.60 \times 10^{-3}$	$6.73 \times 10^{-1}$	$3.11 \times 10^{-3}$
gamma	30	$3.71 \times 10^{-3}$	$3.61 \times 10^{-1}$	$5.82 \times 10^{-3}$
gamma	50	$2.28 \times 10^{-3}$	$1.33 \times 10^{-1}$	$9.84 \times 10^{-3}$
gamma	100	$2.69 \times 10^{-3}$	$7.85 \times 10^{-2}$	$9.19 \times 10^{-3}$
gamma	200	$5.88 \times 10^{-3}$	$8.59 \times 10^{-2}$	$8.56 \times 10^{-3}$
gamma	400	$1.29 \times 10^{-2}$	$9.42 \times 10^{-2}$	$9.27 \times 10^{-3}$
gamma	500	$1.61 \times 10^{-2}$	$9.42 \times 10^{-2}$	$9.62 \times 10^{-3}$
gamma	700	$2.22 \times 10^{-2}$	$9.28 \times 10^{-2}$	$1.02 \times 10^{-2}$
gamma	1000	$2.99 \times 10^{-2}$	$8.73 \times 10^{-2}$	$1.10 \times 10^{-2}$
gamma	1500	$3.99 \times 10^{-2}$	$7.77 \times 10^{-2}$	$1.22 \times 10^{-2}$
gamma	2000	$4.83 \times 10^{-2}$	$7.06 \times 10^{-2}$	$1.31 \times 10^{-2}$
gamma	4000	$6.65 \times 10^{-2}$	$4.86 \times 10^{-2}$	$1.63 \times 10^{-2}$

**Table 4.4b.** The output of running FSOPhantom over an idealized reference banana phantom, consisting of ICRU 4 Tissue for electron sources.

Particle	Energy (keV)	Ellipsoid Mean Dose (pGy)	Absorbed Fraction	Mean Dose Fractional Standard Deviation
e-	10	$3.42 \times 10^{-3}$	$1.00 \times 10^0$	$2.37 \times 10^{-5}$
e-	15	$5.13 \times 10^{-3}$	$1.00 \times 10^0$	$1.90 \times 10^{-5}$
e-	20	$6.84 \times 10^{-3}$	$1.00 \times 10^0$	$3.43 \times 10^{-5}$
e-	30	$1.03 \times 10^{-2}$	$1.00 \times 10^0$	$5.51 \times 10^{-5}$
e-	50	$1.71 \times 10^{-2}$	$9.99 \times 10^{-1}$	$1.02 \times 10^{-4}$
e-	100	$3.42 \times 10^{-2}$	$9.98 \times 10^{-1}$	$1.70 \times 10^{-4}$
e-	200	$6.81 \times 10^{-2}$	$9.94 \times 10^{-1}$	$2.82 \times 10^{-4}$
e-	400	$1.35 \times 10^{-1}$	$9.85 \times 10^{-1}$	$4.67 \times 10^{-4}$
e-	500	$1.67 \times 10^{-1}$	$9.79 \times 10^{-1}$	$5.53 \times 10^{-4}$
e-	700	$2.32 \times 10^{-1}$	$9.68 \times 10^{-1}$	$6.77 \times 10^{-4}$
e-	1000	$3.25 \times 10^{-1}$	$9.50 \times 10^{-1}$	$8.48 \times 10^{-4}$
e-	1500	$4.73 \times 10^{-1}$	$9.22 \times 10^{-1}$	$1.06 \times 10^{-3}$
e-	2000	$6.11 \times 10^{-1}$	$8.93 \times 10^{-1}$	$1.24 \times 10^{-3}$
e-	4000	$1.07 \times 10^0$	$7.85 \times 10^{-1}$	$1.80 \times 10^{-3}$

The model run in this scenario was for sources confined to the internal structure of the reference ellipsoid. The ellipsoid was given a material definition of ICRU 4 component tissue with a total mass of 468 g, which is noted as being far heavier than the average banana. As seen in Table 4.4, The dataset is organized into five columns:

1. Particle: The type of source (either gamma or electron).
2. Energy (keV): The energy level of the particle in kilo-electron volts (keV).
3. Ellipsoid Mean Dose (pGy): The mean absorbed dose by the Ellipsoid object, measured in pico-Grays (pGy).
4. Absorbed Fraction: The fraction of the emitted energy absorbed by the Ellipsoid object.
5. Mean Dose Fractional Standard Deviation: The fractional standard deviation of the mean dose, which represents the variability or uncertainty of the mean dose value.

## Absorbed Fraction for Gamma and Electron Sources in Reference Ellipsoid

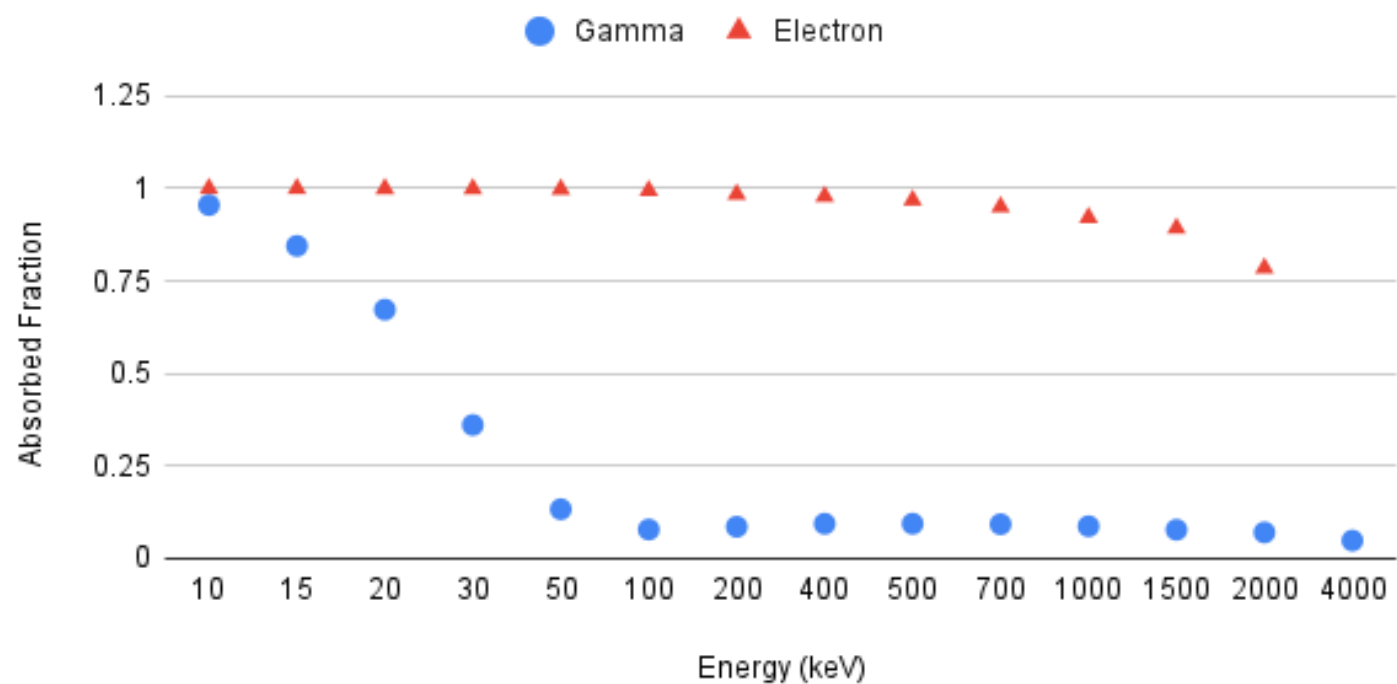


**Figure 4.6.** Absorbed Fractions to reference ellipsoid tissue for gamma and electron sources located in the center of the ellipsoid tissue.

The absorbed fractions (Figure 4.6) for gamma particles vary significantly with energy levels, starting at a high value of 0.955 at 10 keV and decreasing as energy increases, reaching a low value of 0.049 at 4,000 keV. In contrast, the absorbed fractions for electrons remain close to 1 (100% absorption) for lower energy levels and decrease slightly as energy levels increase, with the lowest value of 0.785 at 4,000 keV. The mean dose fractional standard deviation values indicate that the uncertainty in the mean dose measurements is higher for gamma particles than for electrons, especially at higher energy levels.

#### 4.3.2. Three Part Banana Model

Three model runs were processed for a source confined to three separate parts of the banana: the internal tissues, the mesocarp, and the epicarp. All tables follow the format described in the prior section, with additional columns for each respective tissue.

**Table 4.5a.** Mean Dose, Absorbed Fractions for a variety of gamma sources of varying energies initially spawned in the “Internals” tissue.

Particle	Energy (keV)	Epicarp Mean Dose (pGy)	Absorbed Fraction	Mean Dose Fractional Standard Deviation	Mesocarp Mean Dose (pGy)	Absorbed Fraction	Mean Dose Fractional Standard Deviation	Internals Mean Dose (pGy)	Absorbed Fraction	Mean Dose Fractional Standard Deviation
gamma	10	$2.60 \times 10^{-4}$	$1.08 \times 10^{-2}$	$4.28 \times 10^{-2}$	$6.59 \times 10^{-3}$	$3.36 \times 10^{-1}$	$6.29 \times 10^{-3}$	$1.11 \times 10^{-1}$	$6.51 \times 10^{-1}$	$3.27 \times 10^{-3}$
gamma	15	$3.62 \times 10^{-3}$	$1.00 \times 10^{-1}$	$1.34 \times 10^{-2}$	$1.37 \times 10^{-2}$	$4.64 \times 10^{-1}$	$4.80 \times 10^{-3}$	$8.74 \times 10^{-2}$	$3.42 \times 10^{-1}$	$6.19 \times 10^{-3}$
gamma	20	$6.44 \times 10^{-3}$	$1.34 \times 10^{-1}$	$1.13 \times 10^{-2}$	$1.40 \times 10^{-2}$	$3.56 \times 10^{-1}$	$5.98 \times 10^{-3}$	$6.00 \times 10^{-2}$	$1.76 \times 10^{-1}$	$9.60 \times 10^{-3}$
gamma	30	$5.69 \times 10^{-3}$	$7.87 \times 10^{-2}$	$1.50 \times 10^{-2}$	$9.35 \times 10^{-3}$	$1.59 \times 10^{-1}$	$1.01 \times 10^{-2}$	$2.97 \times 10^{-2}$	$5.83 \times 10^{-2}$	$1.74 \times 10^{-2}$
gamma	50	$3.16 \times 10^{-3}$	$2.62 \times 10^{-2}$	$2.46 \times 10^{-2}$	$4.74 \times 10^{-3}$	$4.83 \times 10^{-2}$	$1.71 \times 10^{-2}$	$1.52 \times 10^{-2}$	$1.79 \times 10^{-2}$	$2.78 \times 10^{-2}$
gamma	100	$2.75 \times 10^{-3}$	$1.14 \times 10^{-2}$	$2.69 \times 10^{-2}$	$5.06 \times 10^{-3}$	$2.57 \times 10^{-2}$	$1.61 \times 10^{-2}$	$1.72 \times 10^{-2}$	$1.01 \times 10^{-2}$	$2.37 \times 10^{-2}$
gamma	200	$5.06 \times 10^{-3}$	$1.05 \times 10^{-2}$	$2.44 \times 10^{-2}$	$1.08 \times 10^{-2}$	$2.75 \times 10^{-2}$	$1.52 \times 10^{-2}$	$4.04 \times 10^{-2}$	$1.19 \times 10^{-2}$	$2.28 \times 10^{-2}$
gamma	400	$1.16 \times 10^{-2}$	$1.21 \times 10^{-2}$	$2.60 \times 10^{-2}$	$2.37 \times 10^{-2}$	$3.02 \times 10^{-2}$	$1.65 \times 10^{-2}$	$8.58 \times 10^{-2}$	$1.26 \times 10^{-2}$	$2.57 \times 10^{-2}$
gamma	500	$1.41 \times 10^{-2}$	$1.17 \times 10^{-2}$	$2.74 \times 10^{-2}$	$2.97 \times 10^{-2}$	$3.02 \times 10^{-2}$	$1.71 \times 10^{-2}$	$1.01 \times 10^{-1}$	$1.18 \times 10^{-2}$	$2.73 \times 10^{-2}$
gamma	700	$1.97 \times 10^{-2}$	$1.17 \times 10^{-2}$	$2.85 \times 10^{-2}$	$4.10 \times 10^{-2}$	$2.98 \times 10^{-2}$	$1.81 \times 10^{-2}$	$1.38 \times 10^{-1}$	$1.16 \times 10^{-2}$	$2.87 \times 10^{-2}$
gamma	1000	$2.60 \times 10^{-2}$	$1.08 \times 10^{-2}$	$2.98 \times 10^{-2}$	$5.65 \times 10^{-2}$	$2.88 \times 10^{-2}$	$1.91 \times 10^{-2}$	$1.65 \times 10^{-1}$	$9.72 \times 10^{-3}$	$3.17 \times 10^{-2}$
gamma	1500	$3.53 \times 10^{-2}$	$9.75 \times 10^{-3}$	$3.03 \times 10^{-2}$	$7.53 \times 10^{-2}$	$2.56 \times 10^{-2}$	$2.06 \times 10^{-2}$	$1.74 \times 10^{-1}$	$6.80 \times 10^{-3}$	$3.72 \times 10^{-2}$
gamma	2000	$4.35 \times 10^{-2}$	$9.01 \times 10^{-3}$	$2.96 \times 10^{-2}$	$8.77 \times 10^{-2}$	$2.23 \times 10^{-2}$	$2.19 \times 10^{-2}$	$1.93 \times 10^{-1}$	$5.68 \times 10^{-3}$	$3.92 \times 10^{-2}$
gamma	4000	$6.16 \times 10^{-2}$	$6.38 \times 10^{-3}$	$2.80 \times 10^{-2}$	$1.04 \times 10^{-1}$	$1.32 \times 10^{-2}$	$2.64 \times 10^{-2}$	$1.77 \times 10^{-1}$	$2.60 \times 10^{-3}$	$4.96 \times 10^{-2}$

**Table 4.5b.** Mean Dose, Absorbed Fractions for a variety of electron sources of varying energies initially spawned in the “Internals” tissue. For runs that did not return viable data, ‘-’ is used.

Particle	Energy (keV)	Epicarp Mean Dose (pGy)	Absorbed Fraction	Mean Dose Fractional Standard Deviation	Mesocarp Mean Dose (pGy)	Absorbed Fraction	Mean Dose Fractional Standard Deviation	Internals Mean Dose (pGy)	Absorbed Fraction	Mean Dose Fractional Standard Deviation
e-	10	-	$0.00 \times 10^0$	$0.00 \times 10^0$	$5.81 \times 10^{-6}$	$2.96 \times 10^{-4}$	$2.32 \times 10^{-1}$	$1.70 \times 10^{-1}$	$1.00 \times 10^0$	$7.26 \times 10^{-5}$
e-	15	-	$0.00 \times 10^0$	$0.00 \times 10^0$	$1.68 \times 10^{-5}$	$5.71 \times 10^{-4}$	$1.67 \times 10^{-1}$	$2.55 \times 10^{-1}$	$9.99 \times 10^{-1}$	$1.01 \times 10^{-4}$
e-	20	-	$0.00 \times 10^0$	$0.00 \times 10^0$	$3.70 \times 10^{-5}$	$9.42 \times 10^{-4}$	$1.25 \times 10^{-1}$	$3.40 \times 10^{-1}$	$9.99 \times 10^{-1}$	$1.23 \times 10^{-4}$
e-	30	-	$0.00 \times 10^0$	$0.00 \times 10^0$	$1.11 \times 10^{-4}$	$1.88 \times 10^{-3}$	$8.95 \times 10^{-2}$	$5.09 \times 10^{-1}$	$9.98 \times 10^{-1}$	$1.74 \times 10^{-4}$
e-	50	$1.92 \times 10^{-6}$	$1.59 \times 10^{-5}$	$7.20 \times 10^{-1}$	$4.44 \times 10^{-4}$	$4.52 \times 10^{-3}$	$5.77 \times 10^{-2}$	$8.46 \times 10^{-1}$	$9.95 \times 10^{-1}$	$2.67 \times 10^{-4}$
e-	100	$2.15 \times 10^{-6}$	$8.93 \times 10^{-6}$	$6.95 \times 10^{-1}$	$3.32 \times 10^{-3}$	$1.69 \times 10^{-2}$	$2.97 \times 10^{-2}$	$1.67 \times 10^0$	$9.83 \times 10^{-1}$	$5.14 \times 10^{-4}$
e-	200	$1.39 \times 10^{-5}$	$2.87 \times 10^{-5}$	$2.97 \times 10^{-1}$	$1.90 \times 10^{-2}$	$4.84 \times 10^{-2}$	$1.70 \times 10^{-2}$	$3.24 \times 10^0$	$9.51 \times 10^{-1}$	$8.68 \times 10^{-4}$
e-	400	$8.17 \times 10^{-5}$	$8.47 \times 10^{-5}$	$2.31 \times 10^{-1}$	$1.05 \times 10^{-1}$	$1.34 \times 10^{-1}$	$9.48 \times 10^{-3}$	$5.88 \times 10^0$	$8.64 \times 10^{-1}$	$1.47 \times 10^{-3}$
e-	500	$1.33 \times 10^{-4}$	$1.10 \times 10^{-4}$	$2.44 \times 10^{-1}$	$1.75 \times 10^{-1}$	$1.78 \times 10^{-1}$	$7.87 \times 10^{-3}$	$6.98 \times 10^0$	$8.21 \times 10^{-1}$	$1.71 \times 10^{-3}$
e-	700	$2.21 \times 10^{-4}$	$1.31 \times 10^{-4}$	$2.39 \times 10^{-1}$	$3.65 \times 10^{-1}$	$2.66 \times 10^{-1}$	$5.91 \times 10^{-3}$	$8.72 \times 10^0$	$7.32 \times 10^{-1}$	$2.15 \times 10^{-3}$
e-	1000	$2.38 \times 10^{-3}$	$9.86 \times 10^{-4}$	$8.46 \times 10^{-2}$	$7.57 \times 10^{-1}$	$3.85 \times 10^{-1}$	$4.25 \times 10^{-3}$	$1.04 \times 10^1$	$6.10 \times 10^{-1}$	$2.69 \times 10^{-3}$
e-	1500	$4.80 \times 10^{-2}$	$1.33 \times 10^{-2}$	$2.38 \times 10^{-2}$	$1.50 \times 10^0$	$5.08 \times 10^{-1}$	$2.94 \times 10^{-3}$	$1.21 \times 10^1$	$4.74 \times 10^{-1}$	$3.21 \times 10^{-3}$
e-	2000	$2.20 \times 10^{-1}$	$4.56 \times 10^{-2}$	$1.19 \times 10^{-2}$	$2.24 \times 10^0$	$5.70 \times 10^{-1}$	$2.27 \times 10^{-3}$	$1.26 \times 10^1$	$3.71 \times 10^{-1}$	$3.61 \times 10^{-3}$
e-	4000	$1.42 \times 10^0$	$1.47 \times 10^{-1}$	$3.79 \times 10^{-3}$	$3.49 \times 10^0$	$4.44 \times 10^{-1}$	$2.21 \times 10^{-3}$	$1.30 \times 10^1$	$1.92 \times 10^{-1}$	$4.23 \times 10^{-3}$

As shown in Table 4.5, as the energy of the gammas increases, the absorbed fractions for the epicarp and mesocarp decrease while the absorbed fractions for internal tissues increase. This trend can be attributed to the increasing penetration power of gamma rays at higher energies, allowing them to reach deeper layers of the object.

For electrons, though the most significant increases were observed in the epicarp layer, the absorbed fractions were comparatively lower to the mesocarp and internal layers. This is likely due to the lower penetration power of electrons compared to gamma rays, leading to a higher proportion of energy being absorbed by the outer layers.

The mean dose fractional standard deviation generally decreases for gamma rays as energy increases, indicating a more consistent absorbed dose distribution. However, for electrons, the standard deviation tends to increase with energy, suggesting that the absorbed dose distribution is less consistent at higher energies.

Absorbed Fractions in Tissue Segmentations with Gamma Sources Located in the Internals

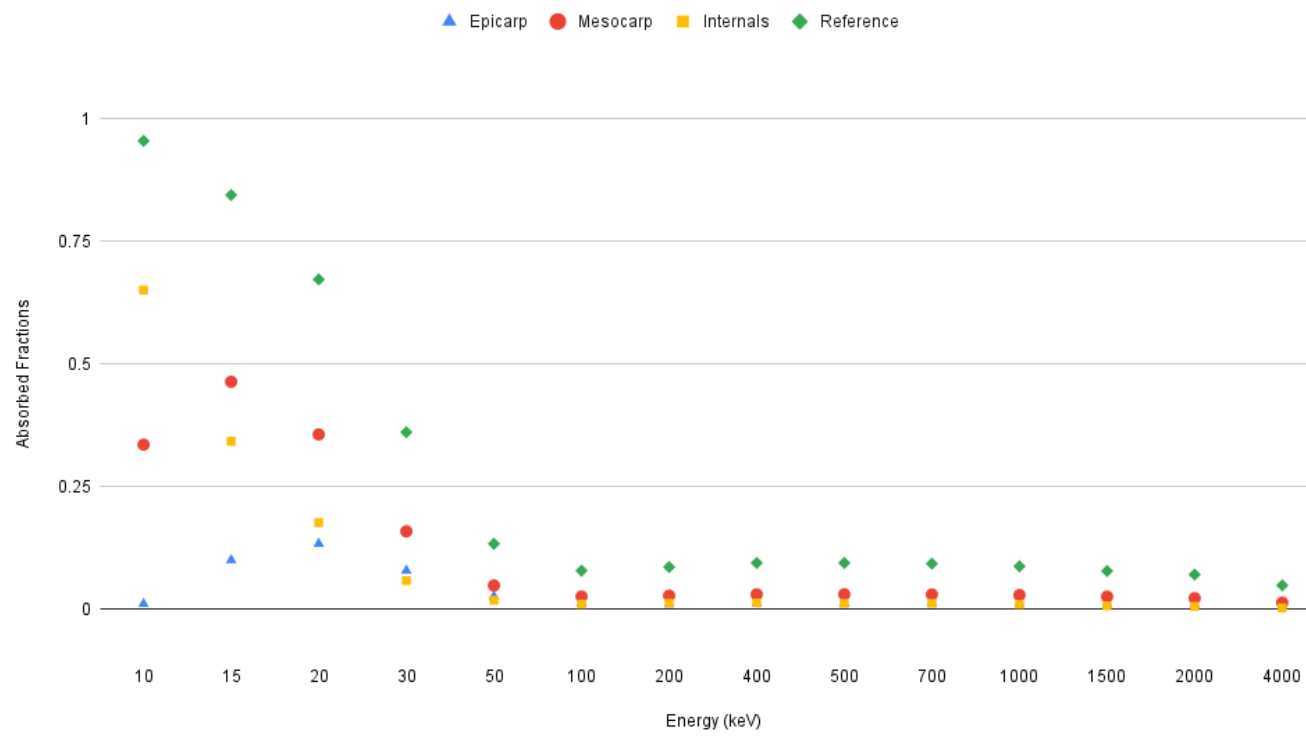


**Figure 4.7.** Absorbed Fractions to various segmented tissues compared to the reference ellipsoidal phantom for gamma sources located in the ‘internals’ tissues.

For gamma particles as energy levels increase, the mean absorbed dose and absorbed fraction values per Figure 4.7 generally decrease for the epicarp and mesocarp but increase for the internals. This suggests that higher-energy gamma particles are more likely to penetrate deeper into the object, resulting in a higher dose for the internals.

Absorbed Fractions in Tissue Segmentations with Electron Sources Located in the Internals

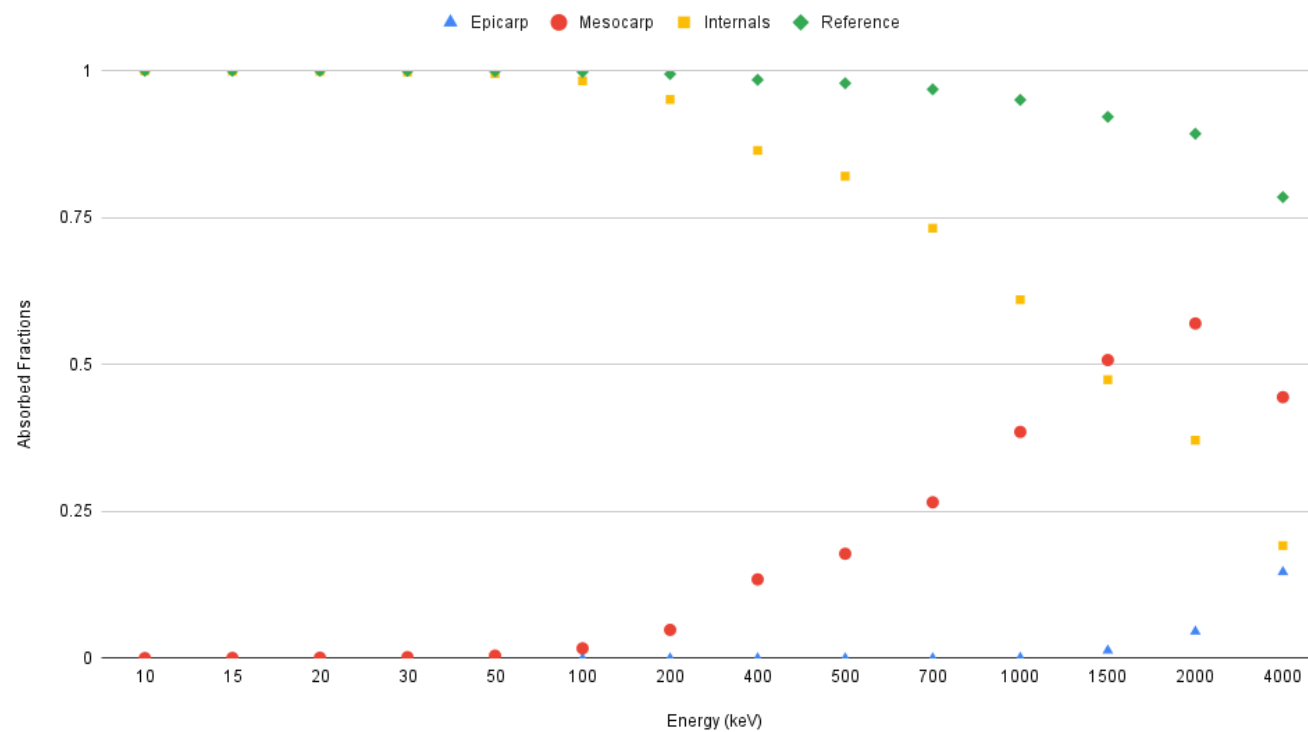


**Figure 4.8.** Absorbed Fractions to various segmented tissues compared to the reference ellipsoidal phantom for electron sources located in the ‘internals’ tissues.

For electron particles, as energy levels increase, the mean absorbed dose values increase for all three components (epicarp, mesocarp, and internals) while the absorbed fraction values generally decrease per Figure 4.8. This indicates that higher-energy electrons deposit more energy in each component, but the fraction of energy absorbed decreases as the energy level increases.

In both cases, the reference ellipsoid generally had a higher absorbed fraction than the respective tissues with significant crossover of data points only occurring for electrons in the region of 10 keV to 100 keV between the reference and the internals segment.

For the scenario of a source in the Mesocarp tissue:

**Table 4.6a.** Mean Dose, Absorbed Fractions for a variety of gamma sources of varying energies initially spawned in the Mesocarp tissue.

Particle	Energy (keV)	Epicarp Mean Dose (pGy)	Absorbed Fraction	Mean Dose Fractional Standard Deviation	Mesocarp Mean Dose (pGy)	Absorbed Fraction	Mean Dose Fractional Standard Deviation	Internals Mean Dose (pGy)	Absorbed Fraction	Mean Dose Fractional Standard Deviation
gamma	10	$2.65 \times 10^{-3}$	$1.10 \times 10^{-1}$	$1.27 \times 10^{-2}$	$1.68 \times 10^{-2}$	$8.54 \times 10^{-1}$	$1.85 \times 10^{-3}$	$4.41 \times 10^{-3}$	$2.59 \times 10^{-2}$	$2.74 \times 10^{-2}$
gamma	15	$7.05 \times 10^{-3}$	$1.95 \times 10^{-1}$	$9.07 \times 10^{-3}$	$1.84 \times 10^{-2}$	$6.25 \times 10^{-1}$	$3.46 \times 10^{-3}$	$8.89 \times 10^{-3}$	$3.49 \times 10^{-2}$	$2.35 \times 10^{-2}$
gamma	20	$8.77 \times 10^{-3}$	$1.82 \times 10^{-1}$	$9.44 \times 10^{-3}$	$1.62 \times 10^{-2}$	$4.12 \times 10^{-1}$	$5.31 \times 10^{-3}$	$8.95 \times 10^{-3}$	$2.63 \times 10^{-2}$	$2.70 \times 10^{-2}$
gamma	30	$6.96 \times 10^{-3}$	$9.62 \times 10^{-2}$	$1.34 \times 10^{-2}$	$9.99 \times 10^{-3}$	$1.70 \times 10^{-1}$	$9.66 \times 10^{-3}$	$5.92 \times 10^{-3}$	$1.16 \times 10^{-2}$	$3.98 \times 10^{-2}$
gamma	50	$3.70 \times 10^{-3}$	$3.07 \times 10^{-2}$	$2.27 \times 10^{-2}$	$5.04 \times 10^{-3}$	$5.14 \times 10^{-2}$	$1.66 \times 10^{-2}$	$3.37 \times 10^{-3}$	$3.97 \times 10^{-3}$	$5.98 \times 10^{-2}$
gamma	100	$3.15 \times 10^{-3}$	$1.30 \times 10^{-2}$	$2.45 \times 10^{-2}$	$5.19 \times 10^{-3}$	$2.64 \times 10^{-2}$	$1.55 \times 10^{-2}$	$3.85 \times 10^{-3}$	$2.27 \times 10^{-3}$	$5.13 \times 10^{-2}$
gamma	200	$5.86 \times 10^{-3}$	$1.22 \times 10^{-2}$	$2.28 \times 10^{-2}$	$1.14 \times 10^{-2}$	$2.91 \times 10^{-2}$	$1.46 \times 10^{-2}$	$9.14 \times 10^{-3}$	$2.69 \times 10^{-3}$	$4.77 \times 10^{-2}$
gamma	400	$1.34 \times 10^{-2}$	$1.39 \times 10^{-2}$	$2.41 \times 10^{-2}$	$2.54 \times 10^{-2}$	$3.24 \times 10^{-2}$	$1.61 \times 10^{-2}$	$1.83 \times 10^{-2}$	$2.69 \times 10^{-3}$	$5.57 \times 10^{-2}$
gamma	500	$1.62 \times 10^{-2}$	$1.35 \times 10^{-2}$	$2.58 \times 10^{-2}$	$3.05 \times 10^{-2}$	$3.10 \times 10^{-2}$	$1.70 \times 10^{-2}$	$2.26 \times 10^{-2}$	$2.66 \times 10^{-3}$	$5.81 \times 10^{-2}$
gamma	700	$2.35 \times 10^{-2}$	$1.39 \times 10^{-2}$	$2.62 \times 10^{-2}$	$4.19 \times 10^{-2}$	$3.05 \times 10^{-2}$	$1.81 \times 10^{-2}$	$3.34 \times 10^{-2}$	$2.81 \times 10^{-3}$	$5.88 \times 10^{-2}$
gamma	1000	$3.04 \times 10^{-2}$	$1.26 \times 10^{-2}$	$2.76 \times 10^{-2}$	$5.32 \times 10^{-2}$	$2.71 \times 10^{-2}$	$1.98 \times 10^{-2}$	$4.48 \times 10^{-2}$	$2.64 \times 10^{-3}$	$6.29 \times 10^{-2}$
gamma	1500	$4.07 \times 10^{-2}$	$1.13 \times 10^{-2}$	$2.84 \times 10^{-2}$	$6.88 \times 10^{-2}$	$2.34 \times 10^{-2}$	$2.17 \times 10^{-2}$	$5.83 \times 10^{-2}$	$2.29 \times 10^{-3}$	$6.42 \times 10^{-2}$
gamma	2000	$4.78 \times 10^{-2}$	$9.91 \times 10^{-3}$	$2.91 \times 10^{-2}$	$8.03 \times 10^{-2}$	$2.04 \times 10^{-2}$	$2.32 \times 10^{-2}$	$7.57 \times 10^{-2}$	$2.23 \times 10^{-3}$	$6.41 \times 10^{-2}$
gamma	4000	$5.96 \times 10^{-2}$	$6.18 \times 10^{-3}$	$3.00 \times 10^{-2}$	$8.71 \times 10^{-2}$	$1.11 \times 10^{-2}$	$2.96 \times 10^{-2}$	$7.88 \times 10^{-2}$	$1.16 \times 10^{-3}$	$7.48 \times 10^{-2}$

**Table 4.6b.** Mean Dose, Absorbed Fractions for a variety of electron sources of varying energies initially spawned in the Mesocarp tissue.

Particle	Energy (keV)	Epicarp Mean Dose (pGy)	Absorbed Fraction	Mean Dose Fractional Standard Deviation	Mesocarp Mean Dose (pGy)	Absorbed Fraction	Mean Dose Fractional Standard Deviation	Internals Mean Dose (pGy)	Absorbed Fraction	Mean Dose Fractional Standard Deviation
e-	10	$2.02 \times 10^{-6}$	$8.38 \times 10^{-5}$	$4.58 \times 10^{-1}$	$1.94 \times 10^{-2}$	$9.88 \times 10^{-1}$	$5.01 \times 10^{-4}$	$2.09 \times 10^{-3}$	$1.23 \times 10^{-2}$	$4.01 \times 10^{-2}$
e-	15	$9.16 \times 10^{-6}$	$2.53 \times 10^{-4}$	$2.44 \times 10^{-1}$	$2.91 \times 10^{-2}$	$9.88 \times 10^{-1}$	$4.98 \times 10^{-4}$	$3.08 \times 10^{-3}$	$1.21 \times 10^{-2}$	$4.04 \times 10^{-2}$
e-	20	$8.47 \times 10^{-6}$	$1.76 \times 10^{-4}$	$2.93 \times 10^{-1}$	$3.88 \times 10^{-2}$	$9.87 \times 10^{-1}$	$5.10 \times 10^{-4}$	$4.32 \times 10^{-3}$	$1.27 \times 10^{-2}$	$3.94 \times 10^{-2}$
e-	30	$3.38 \times 10^{-5}$	$4.67 \times 10^{-4}$	$1.76 \times 10^{-1}$	$5.81 \times 10^{-2}$	$9.87 \times 10^{-1}$	$5.16 \times 10^{-4}$	$6.54 \times 10^{-3}$	$1.28 \times 10^{-2}$	$3.92 \times 10^{-2}$
e-	50	$1.45 \times 10^{-4}$	$1.20 \times 10^{-3}$	$1.13 \times 10^{-1}$	$9.68 \times 10^{-2}$	$9.86 \times 10^{-1}$	$5.24 \times 10^{-4}$	$1.07 \times 10^{-2}$	$1.26 \times 10^{-2}$	$3.94 \times 10^{-2}$
e-	100	$1.07 \times 10^{-3}$	$4.42 \times 10^{-3}$	$5.82 \times 10^{-2}$	$1.93 \times 10^{-1}$	$9.83 \times 10^{-1}$	$5.54 \times 10^{-4}$	$2.04 \times 10^{-2}$	$1.20 \times 10^{-2}$	$4.01 \times 10^{-2}$
e-	200	$6.76 \times 10^{-3}$	$1.40 \times 10^{-2}$	$3.19 \times 10^{-2}$	$3.82 \times 10^{-1}$	$9.73 \times 10^{-1}$	$6.76 \times 10^{-4}$	$4.28 \times 10^{-2}$	$1.26 \times 10^{-2}$	$3.84 \times 10^{-2}$
e-	400	$3.93 \times 10^{-2}$	$4.07 \times 10^{-2}$	$1.83 \times 10^{-2}$	$7.41 \times 10^{-1}$	$9.43 \times 10^{-1}$	$9.35 \times 10^{-4}$	$1.04 \times 10^{-1}$	$1.52 \times 10^{-2}$	$3.22 \times 10^{-2}$
e-	500	$6.66 \times 10^{-2}$	$5.52 \times 10^{-2}$	$1.55 \times 10^{-2}$	$9.10 \times 10^{-1}$	$9.27 \times 10^{-1}$	$1.05 \times 10^{-3}$	$1.38 \times 10^{-1}$	$1.63 \times 10^{-2}$	$2.99 \times 10^{-2}$
e-	700	$1.42 \times 10^{-1}$	$8.40 \times 10^{-2}$	$1.22 \times 10^{-2}$	$1.23 \times 10^0$	$8.92 \times 10^{-1}$	$1.26 \times 10^{-3}$	$2.51 \times 10^{-1}$	$2.11 \times 10^{-2}$	$2.50 \times 10^{-2}$
e-	1000	$3.03 \times 10^{-1}$	$1.26 \times 10^{-1}$	$9.37 \times 10^{-3}$	$1.64 \times 10^0$	$8.36 \times 10^{-1}$	$1.56 \times 10^{-3}$	$5.17 \times 10^{-1}$	$3.04 \times 10^{-2}$	$2.00 \times 10^{-2}$
e-	1500	$6.04 \times 10^{-1}$	$1.67 \times 10^{-1}$	$7.00 \times 10^{-3}$	$2.21 \times 10^0$	$7.49 \times 10^{-1}$	$1.94 \times 10^{-3}$	$1.11 \times 10^0$	$4.37 \times 10^{-2}$	$1.55 \times 10^{-2}$
e-	2000	$8.98 \times 10^{-1}$	$1.86 \times 10^{-1}$	$5.74 \times 10^{-3}$	$2.62 \times 10^0$	$6.66 \times 10^{-1}$	$2.26 \times 10^{-3}$	$1.78 \times 10^0$	$5.23 \times 10^{-2}$	$1.34 \times 10^{-2}$
e-	4000	$1.66 \times 10^0$	$1.72 \times 10^{-1}$	$3.84 \times 10^{-3}$	$3.53 \times 10^0$	$4.49 \times 10^{-1}$	$3.02 \times 10^{-3}$	$2.88 \times 10^0$	$4.23 \times 10^{-2}$	$1.22 \times 10^{-2}$

In summary of Table 4.6, as the energy of gammas increases, the epicarp mean dose increases throughout the dataset. The absorbed fraction shows a decreasing trend while the mean dose fractional standard deviation remains relatively constant. For electrons, the epicarp mean dose increases as the energy increases with a much more pronounced increase at higher energy levels. The absorbed fraction increases while the mean dose fractional standard deviation decreases with increasing energy.

Comparing the two particle types, gamma rays generally have a higher epicarp absorbed fraction than electrons at lower energy levels, but this trend reverses as the energy increases. In terms of mean dose fractional standard deviation, gamma rays have lower values than electrons across all energy levels. In mesocarp and internals, the mean doses for both gamma rays and electrons increase with energy. However, the absorbed fractions for gamma rays decrease with increasing energy, while for electrons, the absorbed fractions remain relatively constant, with only slight decreases as energy increases near the end of the tested range. The mean dose fractional standard deviations for both gamma rays and electrons show a general increase with increasing energy in mesocarp and internals, with gamma rays having lower values than electrons across all energy levels.

## Absorbed Fractions in Tissue Segmentations with Gamma Sources Located in the Mesocarp

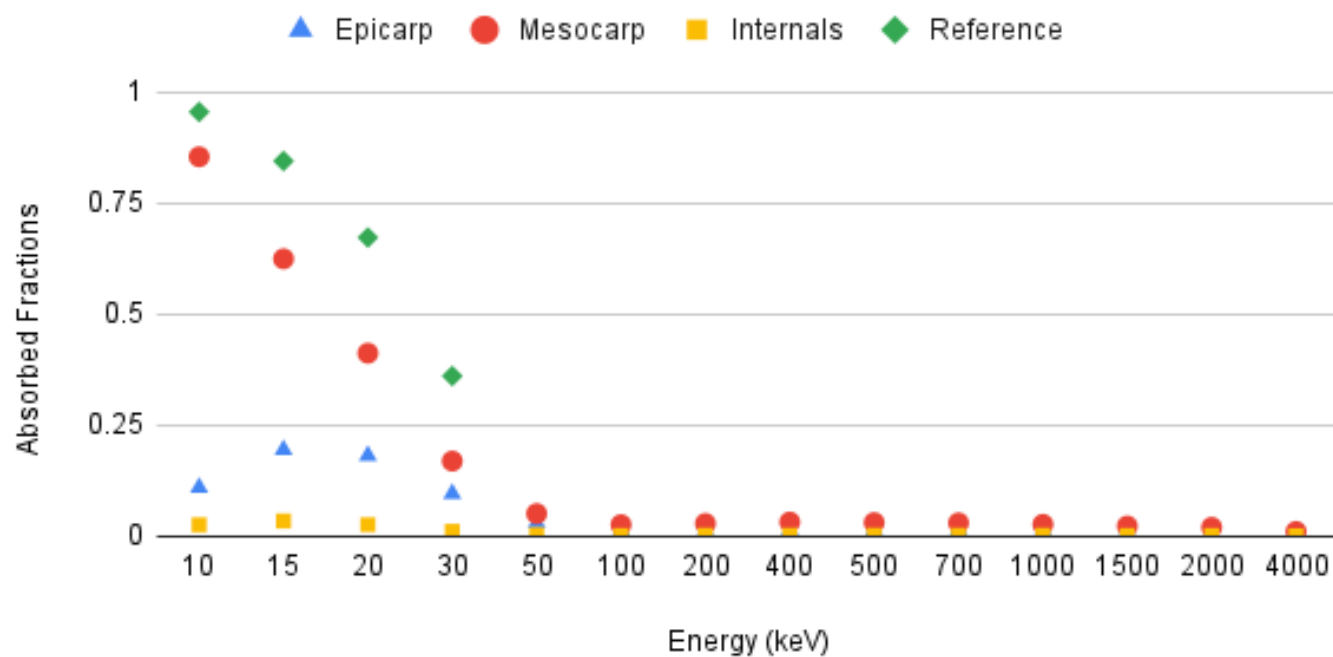


**Figure 4.9.** Absorbed Fractions to various segmented tissues compared to the reference ellipsoidal phantom for gamma sources located in the mesocarp tissues.

The reference ellipsoid still maintains a larger absorbed fraction up to 50 keV, per Figure 4.9, with the mesocarp having the closest absorbed fraction values, and significantly higher than that of the internals or epicarp. However, after 50 keV, there is generally strong evidence for agreement between absorbed fraction values.

## Absorbed Fractions in Tissue Segmentations with Electron Sources Located in the Mesocarp

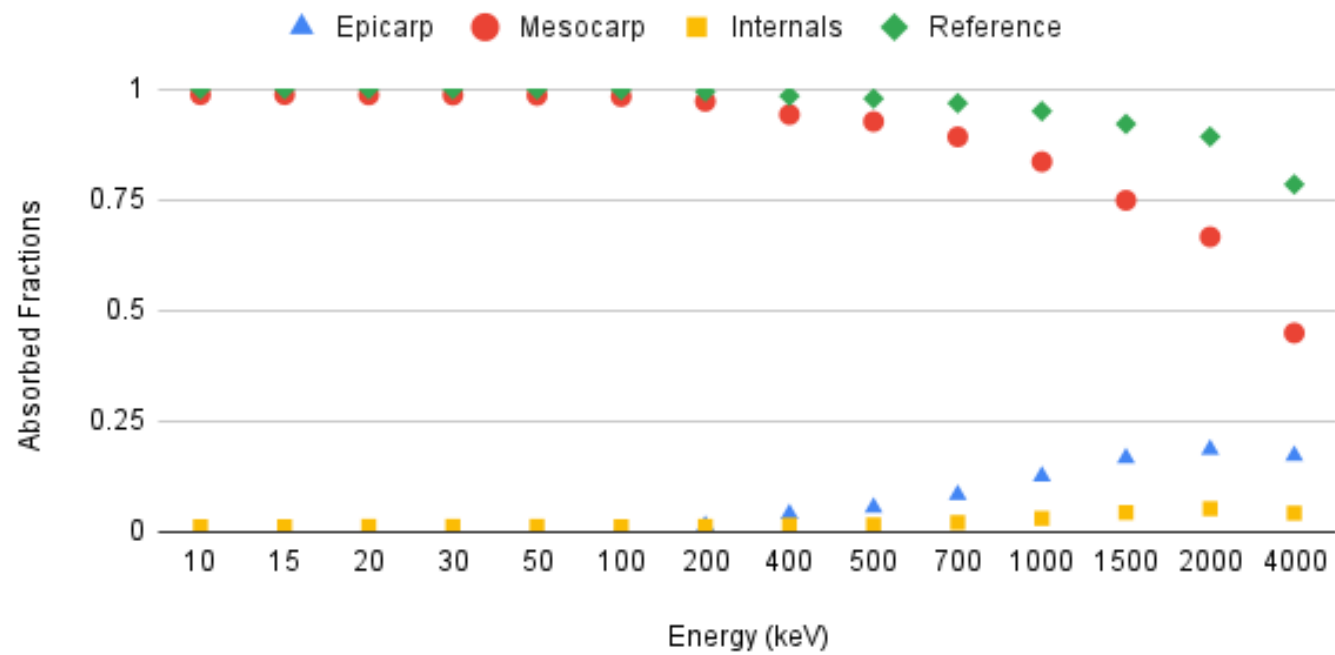


**Figure 4.10.** Absorbed Fractions to various segmented tissues compared to the reference ellipsoidal phantom for electron sources located in the mesocarp tissues.

For electrons, per Figure 4.10, the absorbed fractions in the Epicarp component are the lowest among the three components, while the absorbed fractions in the Mesocarp and Internals components are closer to each other and remain high (above 0.6) at higher energy levels. This time, it is the mesocarp that remains closest to the reference ellipsoid.

Finally, observing the scenario of a source located in the epicarp:

**Table 4.7a.** Mean Dose, Absorbed Fractions for a variety of gamma sources of varying energies initially spawned in the epicarp tissue.

Particle	Energy (keV)	Epicarp Mean Dose (pGy)	Absorbed Fraction	Mean Dose Fractional Standard Deviation	Mesocarp Mean Dose (pGy)	Absorbed Fraction	Mean Dose Fractional Standard Deviation	Internals Mean Dose (pGy)	Absorbed Fraction	Mean Dose Fractional Standard Deviation
gamma	10	$1.88 \times 10^{-2}$	$7.78 \times 10^{-1}$	$2.39 \times 10^{-3}$	$1.69 \times 10^{-3}$	$8.61 \times 10^{-2}$	$1.46 \times 10^{-2}$	$8.50 \times 10^{-5}$	$5.00 \times 10^{-4}$	$2.00 \times 10^{-1}$
gamma	15	$1.85 \times 10^{-2}$	$5.11 \times 10^{-1}$	$4.37 \times 10^{-3}$	$4.68 \times 10^{-3}$	$1.59 \times 10^{-1}$	$1.03 \times 10^{-2}$	$1.59 \times 10^{-3}$	$6.23 \times 10^{-3}$	$5.63 \times 10^{-2}$
gamma	20	$1.61 \times 10^{-2}$	$3.35 \times 10^{-1}$	$6.28 \times 10^{-3}$	$5.84 \times 10^{-3}$	$1.49 \times 10^{-1}$	$1.06 \times 10^{-2}$	$2.66 \times 10^{-3}$	$7.81 \times 10^{-3}$	$5.00 \times 10^{-2}$
gamma	30	$1.03 \times 10^{-2}$	$1.42 \times 10^{-1}$	$1.08 \times 10^{-2}$	$4.49 \times 10^{-3}$	$7.63 \times 10^{-2}$	$1.52 \times 10^{-2}$	$2.65 \times 10^{-3}$	$5.20 \times 10^{-3}$	$5.99 \times 10^{-2}$
gamma	50	$4.95 \times 10^{-3}$	$4.11 \times 10^{-2}$	$1.95 \times 10^{-2}$	$2.52 \times 10^{-3}$	$2.56 \times 10^{-2}$	$2.39 \times 10^{-2}$	$1.30 \times 10^{-3}$	$1.53 \times 10^{-3}$	$9.44 \times 10^{-2}$
gamma	100	$4.29 \times 10^{-3}$	$1.78 \times 10^{-2}$	$2.04 \times 10^{-2}$	$2.66 \times 10^{-3}$	$1.35 \times 10^{-2}$	$2.22 \times 10^{-2}$	$2.04 \times 10^{-3}$	$1.20 \times 10^{-3}$	$6.96 \times 10^{-2}$
gamma	200	$8.61 \times 10^{-3}$	$1.78 \times 10^{-2}$	$1.88 \times 10^{-2}$	$6.01 \times 10^{-3}$	$1.53 \times 10^{-2}$	$2.05 \times 10^{-2}$	$4.40 \times 10^{-3}$	$1.29 \times 10^{-3}$	$6.85 \times 10^{-2}$
gamma	400	$1.86 \times 10^{-2}$	$1.93 \times 10^{-2}$	$2.05 \times 10^{-2}$	$1.33 \times 10^{-2}$	$1.69 \times 10^{-2}$	$2.23 \times 10^{-2}$	$9.56 \times 10^{-3}$	$1.40 \times 10^{-3}$	$7.82 \times 10^{-2}$
gamma	500	$2.37 \times 10^{-2}$	$1.96 \times 10^{-2}$	$2.11 \times 10^{-2}$	$1.65 \times 10^{-2}$	$1.68 \times 10^{-2}$	$2.33 \times 10^{-2}$	$1.15 \times 10^{-2}$	$1.35 \times 10^{-3}$	$8.15 \times 10^{-2}$
gamma	700	$3.19 \times 10^{-2}$	$1.89 \times 10^{-2}$	$2.26 \times 10^{-2}$	$2.26 \times 10^{-2}$	$1.64 \times 10^{-2}$	$2.46 \times 10^{-2}$	$1.45 \times 10^{-2}$	$1.21 \times 10^{-3}$	$8.75 \times 10^{-2}$
gamma	1000	$3.91 \times 10^{-2}$	$1.62 \times 10^{-2}$	$2.46 \times 10^{-2}$	$3.16 \times 10^{-2}$	$1.61 \times 10^{-2}$	$2.59 \times 10^{-2}$	$2.17 \times 10^{-2}$	$1.27 \times 10^{-3}$	$8.85 \times 10^{-2}$
gamma	1500	$4.47 \times 10^{-2}$	$1.23 \times 10^{-2}$	$2.79 \times 10^{-2}$	$4.24 \times 10^{-2}$	$1.44 \times 10^{-2}$	$2.80 \times 10^{-2}$	$2.87 \times 10^{-2}$	$1.13 \times 10^{-3}$	$9.24 \times 10^{-2}$
gamma	2000	$5.16 \times 10^{-2}$	$1.07 \times 10^{-2}$	$2.90 \times 10^{-2}$	$5.24 \times 10^{-2}$	$1.33 \times 10^{-2}$	$2.92 \times 10^{-2}$	$3.26 \times 10^{-2}$	$9.59 \times 10^{-4}$	$9.60 \times 10^{-2}$
gamma	4000	$6.20 \times 10^{-2}$	$6.42 \times 10^{-3}$	$3.22 \times 10^{-2}$	$6.51 \times 10^{-2}$	$8.29 \times 10^{-3}$	$3.53 \times 10^{-2}$	$5.67 \times 10^{-2}$	$8.33 \times 10^{-4}$	$8.74 \times 10^{-2}$

**Table 4.7b.** Mean Dose, Absorbed Fractions for a variety of electron sources of varying energies initially spawned in the epicarp tissue. For runs that did not return viable data, '-' is used.

Particle	Energy (keV)	Epicarp Mean Dose (pGy)	Absorbed Fraction	Mean Dose Fractional Standard Deviation	Mesocarp Mean Dose (pGy)	Absorbed Fraction	Mean Dose Fractional Standard Deviation	Internals Mean Dose (pGy)	Absorbed Fraction	Mean Dose Fractional Standard Deviation
e-	10	$2.41 \times 10^{-2}$	$9.99 \times 10^{-1}$	$1.71 \times 10^{-4}$	$2.66 \times 10^{-5}$	$1.36 \times 10^{-3}$	$1.21 \times 10^{-1}$	-	-	-
e-	15	$3.61 \times 10^{-2}$	$9.98 \times 10^{-1}$	$1.78 \times 10^{-4}$	$4.16 \times 10^{-5}$	$1.41 \times 10^{-3}$	$1.19 \times 10^{-1}$	-	-	-
e-	20	$4.81 \times 10^{-2}$	$9.98 \times 10^{-1}$	$1.86 \times 10^{-4}$	$5.29 \times 10^{-5}$	$1.35 \times 10^{-3}$	$1.20 \times 10^{-1}$	-	-	-
e-	30	$7.21 \times 10^{-2}$	$9.97 \times 10^{-1}$	$2.26 \times 10^{-4}$	$1.05 \times 10^{-4}$	$1.79 \times 10^{-3}$	$1.04 \times 10^{-1}$	-	-	-
e-	50	$1.20 \times 10^{-1}$	$9.96 \times 10^{-1}$	$2.58 \times 10^{-4}$	$1.62 \times 10^{-4}$	$1.65 \times 10^{-3}$	$1.04 \times 10^{-1}$	$1.44 \times 10^{-5}$	$1.69 \times 10^{-5}$	$1.00 \times 10^0$
e-	100	$2.38 \times 10^{-1}$	$9.88 \times 10^{-1}$	$4.21 \times 10^{-4}$	$6.38 \times 10^{-4}$	$3.25 \times 10^{-3}$	$6.92 \times 10^{-2}$	$7.40 \times 10^{-6}$	$4.35 \times 10^{-6}$	$1.00 \times 10^0$
e-	200	$4.63 \times 10^{-1}$	$9.60 \times 10^{-1}$	$7.78 \times 10^{-4}$	$4.86 \times 10^{-3}$	$1.24 \times 10^{-2}$	$3.35 \times 10^{-2}$	$1.29 \times 10^{-5}$	$3.79 \times 10^{-6}$	$6.95 \times 10^{-1}$
e-	400	$8.53 \times 10^{-1}$	$8.84 \times 10^{-1}$	$1.35 \times 10^{-3}$	$3.36 \times 10^{-2}$	$4.28 \times 10^{-2}$	$1.75 \times 10^{-2}$	$2.54 \times 10^{-5}$	$3.74 \times 10^{-6}$	$6.25 \times 10^{-1}$
e-	500	$1.01 \times 10^0$	$8.40 \times 10^{-1}$	$1.60 \times 10^{-3}$	$5.84 \times 10^{-2}$	$5.94 \times 10^{-2}$	$1.46 \times 10^{-2}$	$3.16 \times 10^{-4}$	$3.72 \times 10^{-5}$	$5.74 \times 10^{-1}$
e-	700	$1.26 \times 10^0$	$7.49 \times 10^{-1}$	$2.04 \times 10^{-3}$	$1.32 \times 10^{-1}$	$9.58 \times 10^{-2}$	$1.11 \times 10^{-2}$	$1.78 \times 10^{-4}$	$1.50 \times 10^{-5}$	$6.13 \times 10^{-1}$
e-	1000	$1.50 \times 10^0$	$6.23 \times 10^{-1}$	$2.58 \times 10^{-3}$	$2.82 \times 10^{-1}$	$1.43 \times 10^{-1}$	$8.75 \times 10^{-3}$	$1.05 \times 10^{-3}$	$6.16 \times 10^{-5}$	$3.14 \times 10^{-1}$
e-	1500	$1.74 \times 10^0$	$4.80 \times 10^{-1}$	$3.16 \times 10^{-3}$	$5.76 \times 10^{-1}$	$1.95 \times 10^{-1}$	$7.26 \times 10^{-3}$	$2.65 \times 10^{-2}$	$1.04 \times 10^{-3}$	$8.57 \times 10^{-2}$
e-	2000	$1.91 \times 10^0$	$3.95 \times 10^{-1}$	$3.49 \times 10^{-3}$	$8.54 \times 10^{-1}$	$2.17 \times 10^{-1}$	$6.82 \times 10^{-3}$	$1.42 \times 10^{-1}$	$4.17 \times 10^{-3}$	$4.11 \times 10^{-2}$
e-	4000	$2.38 \times 10^0$	$2.47 \times 10^{-1}$	$4.00 \times 10^{-3}$	$1.67 \times 10^0$	$2.12 \times 10^{-1}$	$6.70 \times 10^{-3}$	$1.15 \times 10^0$	$1.69 \times 10^{-2}$	$1.89 \times 10^{-2}$

In summary of Table 4.7, for gamma sources Epicarp Mean Dose and Absorbed Fraction values generally decrease as energy levels increase. The Mean Dose Fractional Standard Deviation values show a slight increasing trend as the energy levels increase. Mesocarp Mean Dose values first increase and then decrease as energy levels increase, while Absorbed Fraction values follow a similar trend. The Mean Dose Fractional Standard Deviation values show a slight increasing trend as energy levels increase. The Internals Mean Dose values increase with increasing energy levels, while Absorbed Fraction values remain relatively stable. The Mean Dose Fractional Standard Deviation values show a decreasing trend as energy levels increase.

For electron sources, Epicarp Mean Dose values increase with increasing energy levels, and the Absorbed Fraction values decrease as energy levels increase. The Mean Dose Fractional Standard Deviation values also show an increasing trend with increasing energy levels. Mesocarp Mean Dose values increase with increasing energy levels, and the Absorbed Fraction values decrease as energy levels increase. The Mean Dose Fractional Standard Deviation values show a decreasing trend as energy levels increase. The Internals Mean Dose values increase with increasing energy levels, while Absorbed Fraction values remain relatively stable. The Mean Dose Fractional Standard Deviation values show a decreasing trend as energy levels increase.

## Absorbed Fractions in Tissue Segmentations with Gamma Sources Located in the Epicarp

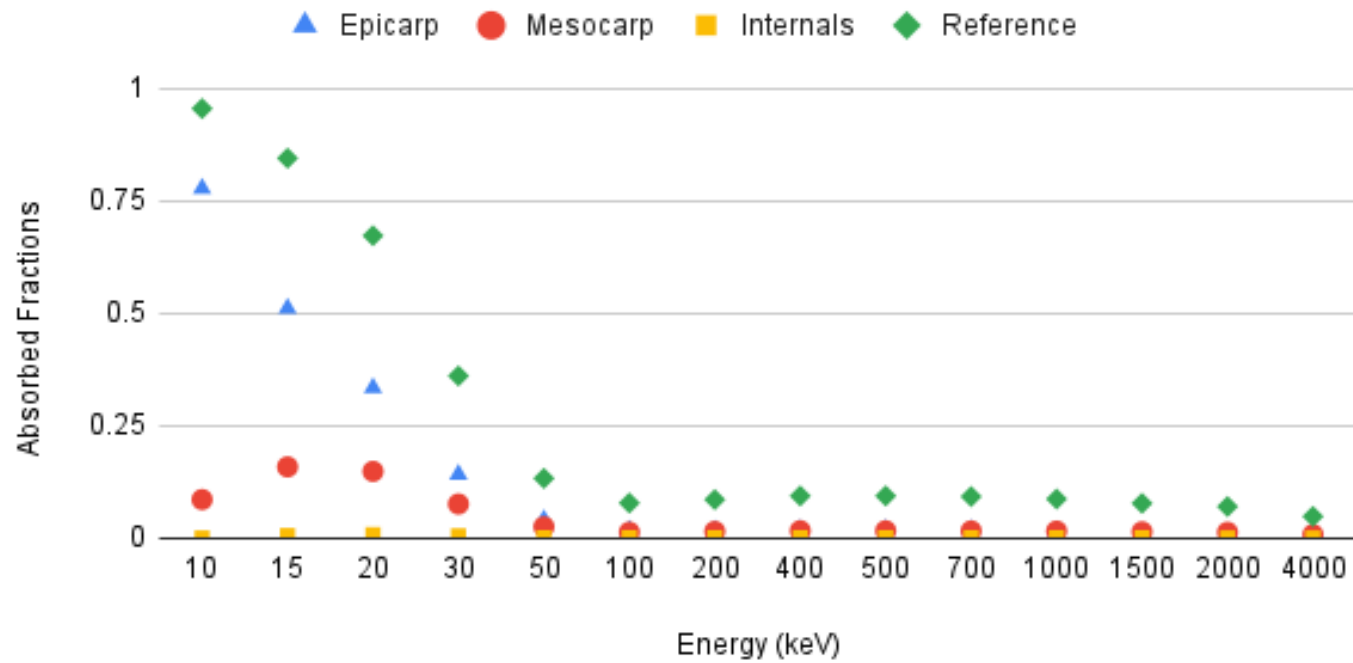


**Figure 4.11.** Absorbed Fractions to various segmented tissues compared to the reference ellipsoidal phantom for gamma sources located in the epicarp tissues.

The reference ellipsoid again maintains a larger absorbed fraction, per Figure 4.11, with the epicarp having the closest absorbed fraction values. The epicarp has a significantly higher absorbed fraction than the internals or mesocarp until 50 keV. After which there is generally strong evidence for agreement between absorbed fraction values between the distinct tissue, but the reference ellipsoid still dominates.

## Absorbed Fractions in Tissue Segmentations with Electron Sources Located in the Epicarp

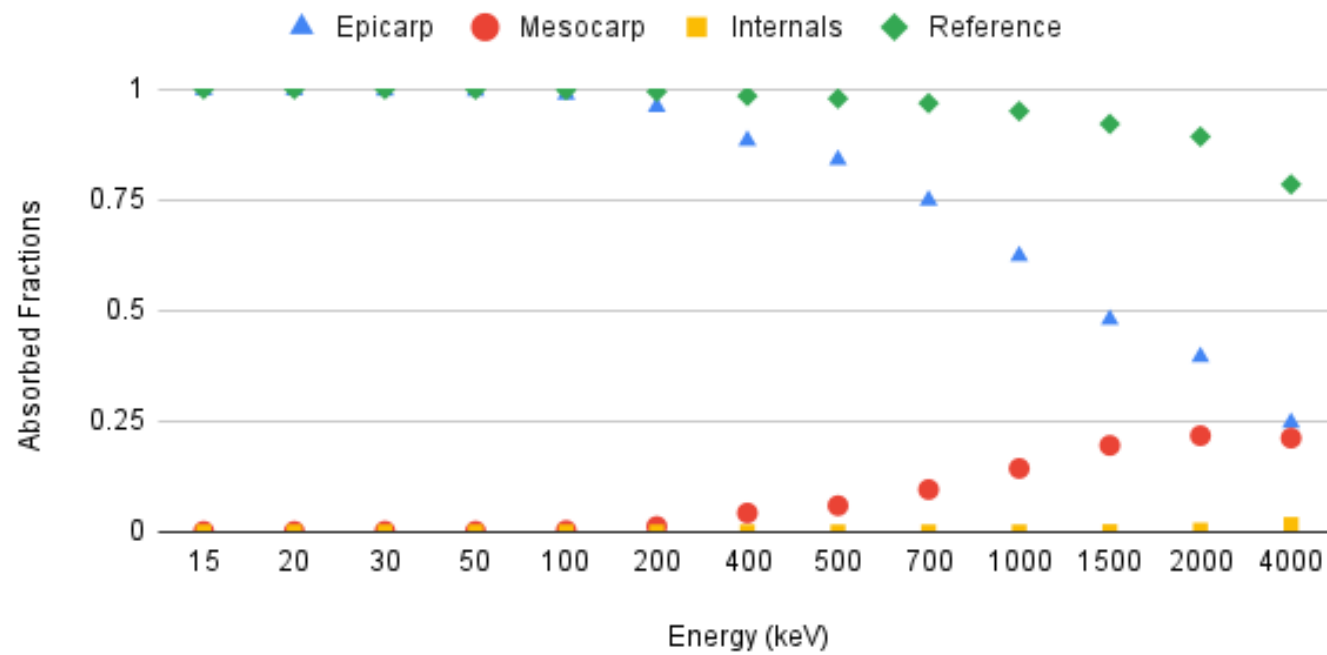


**Figure 4.12.** Absorbed Fractions to various segmented tissues compared to the reference ellipsoidal phantom for electron sources located in the epicarp tissues.

For electrons, per Figure 4.12, the absorbed fractions in the Epicarp component are the highest among the three components. While the absorbed fractions in the Mesocarp and Internals components are closer to each other up to 400 keV, where they begin to diverge at higher energy levels with the mesocarp meeting the epicarp at 4000 keV. The epicarp remains closest to the reference ellipsoid up to 200 keV.

#### 4.4 CONCLUSION

In conclusion, this study has demonstrated the efficacy of an open-source dosimetric phantom program, FSOPhantom, in analyzing the absorbed radiation dose for different layers of a simulated banana when exposed to both gamma and electron sources. The program's ability to generate detailed data on absorbed fractions, mean doses, and fractional standard deviations across a wide range of radiation energies highlights its versatility and usefulness in radiation dosimetry applications. Furthermore, our analysis of the generated data has revealed distinct trends in the behavior of gamma rays and electrons as their energies increase, which provides valuable insight into the interactions between radiation and the simulated banana object. The findings support the notion that gamma rays possess higher penetration power compared to electrons, leading to a more consistent absorbed dose distribution at higher energies. While this data is biologically obvious, this is the first time such analysis has been performed on the banana.

The study also emphasizes the importance of comparing the results obtained from ellipsoid approximation models and biologically accurate

models in radiation dosimetry research. The differences between these two types of models could significantly impact the accuracy of dose estimations, particularly in cases where the subject of interest exhibits complex geometries and heterogeneities.

Overall, the successful application of the open-source dosimetric phantom program in this study not only validates its performance, but also contributes to the growing body of knowledge in radiation dosimetry. This work highlights the potential of such programs in improving the understanding of radiation interactions with various materials and biological systems, ultimately paving the way for more accurate and reliable dosimetric assessments in the future.

#### 4.5 ACKNOWLEDGEMENTS

Andrew Ellison of Boston University Medical School for high fidelity CT scans of many types of flora. The author happily presents the public facing pathway to their work: <http://insideinsides.blogspot.com/>

## REFERENCES

- Agostinelli S, et al. Geant4 - A Simulation Toolkit. Nucl Instrum Meth A. 2003;506:250-303.
- Allison J, et al. Recent Developments in Geant4. Nucl Instrum Meth A. 2016;835:186-225.
- Allison J, et al. Geant4 Developments and Applications. IEEE Trans Nucl Sci. 2006;53:270-278.
- Anhwange B, Ugye J, Nyiatagher TD. Chemical Composition of Musa sepientum (Banana) Peels. Electron J Environ Agric Food Chem. 2009;8:437-4442.
- Autodesk, inc. Autodesk Meshmixer. 2018. Available from:  
<https://meshmixer.com/>
- Biermans G, Horemans N, Hens N, Batlle JV, Vandenhove H, Cuypers A. A dynamic dosimetry model for radioactive exposure scenarios in Arabidopsis thaliana. J Theor Biol. 2014;347:54-62.  
doi:10.1016/j.jtbi.2014.01.012
- Caffrey EA, Johansen MP, Higley KA. Voxel modeling of rabbits for use in radiological dose rate calculations. J Environ Radioact. 2016;151(2):480-486. doi:10.1016/j.jenvrad.2015.04.008
- Condon C. Pine Tree Dosimetry: Development of Geometric and Compositionally Specific Sectional Models for Organ Dose Assessment. Oregon State University; 2019. Available from:

[https://ir.library.oregonstate.edu/concern/graduate\\_thesis\\_or\\_dissertations/000005176](https://ir.library.oregonstate.edu/concern/graduate_thesis_or_dissertations/000005176)

Fedorov A, Beichel R, Kalpathy-Cramer J, Finet J, Fillion-Robin J-C, Pujol S, et al. 3D Slicer as an Image Computing Platform for the Quantitative Imaging Network. *Magn Reson Imaging*. 2012 Nov;30(9):1323-41. doi: 10.1016/j.mri.2012.05.001. PMID: 22770690. PMCID: PMC3466397.

ICRP. Environmental Protection - the Concept and Use of Reference Animals and Plants. ICRP Publication 108. *Ann ICRP*. 2008;38(4-6).

ICRP. Conversion Coefficients for Radiological Protection Quantities for External Radiation Exposures. ICRP Publication 116, *Ann ICRP*. 2010;40(2-5).

ICRP. Dose coefficients for nonhuman biota environmentally exposed to radiation. ICRP Publication 136. *Ann ICRP*. 2017;46(2).

Langdon R. *The Journal of Pacific History*. 1993;28(1):15-35.

Mansfield G. Banana Equivalent Dose. *RadSafe Mailing List*; 1995.

Montgomery DA, Martinez NE. Dosimetric modeling of Tc-99, Cs-137, Np-237, and U-238 in the grass species *Andropogon Virginicus*: Development and comparison of stylized, voxel, and hybrid phantom geometry. *J Environ Radioact*. 2020;211:106075. Neville D. *Faster, Sharper and Open: A New Pipeline for Biota Phantom Creation*. Oregon State University; 2019. Available from: [https://ir.library.oregonstate.edu/concern/graduate\\_thesis\\_or\\_dissertations/9k41zm466](https://ir.library.oregonstate.edu/concern/graduate_thesis_or_dissertations/9k41zm466)

- Pereira L de O, Gama Filho HS, Luiz L da C, Batista RT, Ferreira DS, Gonçalves EA de S, et al. Elementary analysis in banana samples using X-Ray Fluorescence. *Res Soc Dev.* 2021;10(11):e565101119667. doi:10.33448/rsd-v10i11.19667
- Ruedig E, Beresford NA, Gomez Fernandez ME, Higley K. A comparison of the ellipsoidal and voxelized dosimetric methodologies for internal, heterogeneous radionuclide sources. *J Environ Radioact.* 2015;140:70-77. doi:10.1016/j.jenvrad.2014.11.004
- Soltani Firouz M, Alimardani R, Omid M. Some physical properties of full-ripe banana fruit (Cavendish variety). *Int J Agric Sci Res Technol (IJASRT).* 2011;1:1-5.
- Xu XG. An exponential growth of computational phantom research in radiation protection, imaging, and radiotherapy: a review of the fifty-year history. *Phys Med Biol.* 2014 Sep 21;59(18):R233-302. doi:10.1088/0031-9155/59/18/R233. PMID: 25144730; PMCID: PMC4169876.
- Yoschenko VI, Kashparov VA, Melnychuk MD, Levchuk SE, Bondar YO, Lazarev M, et al. Chronic Irradiation Of Scots Pine Trees (*Pinus Sylvestris*) In The Chernobyl Exclusion Zone: Dosimetry And Radiobiological Effects. *Health Phys.* 2011;101(4):393-408. doi:10.1097/hp.0b013e3182118094doi:10.1016/j.jenvrad.2019.106075

## Chapter 5: General Summary and Conclusions

This dissertation sought to provide a glimpse into the emerging topics and technologies facing the radiation ecology community. In an era marked undeniably by climate change, it is now crucially important that knowledge is paired with the tools of our time to ensure the efficacy and efficiency of our stewardship of this world we call home.

The study on phytostabilization and phytoremediation revealed that plant species such as *H. petiolaris*, *S. airoides*, and *K. scoparia* possess distinct characteristics that make them suitable for specific regions and conditions. The complex interplay between soil characteristics and plant uptake highlights the importance of selecting appropriate species for reclamation efforts. Despite challenges posed by arid region soils, the potential for low-cost and environmentally friendly techniques remains crucial for the well-being of surrounding communities and biodiversity.

The analysis of in situ dose rates from contaminated growth media showed significant deviations compared to the proposed values in the ICRP guidelines. These discrepancies underscore the need for refining the RAPs approach and dose coefficients based on in situ data. Further investigation into the complex relationship between radionuclide uptake and soil characteristics is warranted to develop a more accurate and site-specific radiological protection framework.

Lastly, the study on FSOPhantom showcased its versatility in analyzing absorbed radiation doses for different layers of a simulated banana when exposed to gamma and electron sources. The program's ability to

generate detailed data on absorbed fractions and mean doses across a wide range of radiation energies highlights its usefulness in radiation dosimetry applications. The differences between ellipsoid approximation models and biologically accurate models in dosimetry research were also emphasized, as these differences could significantly impact the accuracy of dose estimations.

This dissertation seeks to contribute to the ever-growing body of knowledge in phytoremediation, environmental radiological protection, and radiation dosimetry. With hope, this work can ultimately pave the way for more accurate and reliable assessments and sustainable solutions in each respective field to ensure the ecology of our world can be supported for generations to come.